Elevated temperature fatally disrupts nuclear divisions in the early *Drosophila* embryo.

Girish Kale[1,*], Pratika Agarwal[1], J Jaime Diaz-Larrosa[1], Steffen Lemke[1,2,*]

[1] Centre for Organismal Studies, University of Heidelberg, Heidelberg. Germany
[2] Institute of Biology, University of Hohenheim, Stuttgart, Germany
* Correspondance: G.K. (girish.kale@cos.uni-heidelberg.de), S.L. (steffen.lemke@uni-hohenheim.de)

Abstract:

Temperature fluctuations can challenge animal survival, especially in embryos of animals that can't actively regulate their body temperature. Previous work in insects suggests that spatial gradients and temporal variations in temperature can affect embryonic development in a region-specific manner. Yet, it is unclear if elevated temperature produces developmental defects, and if so, how the disruption may manifest. Here we use early embryonic development of the fruit fly *Drosophila melanogaster* as a model to address consequences of elevated temperature on fly embryonic development.

We identified the syncytial blastoderm stage as a critical time window, being particularly sensitive to elevated temperature. The syncytial blastoderm stage involves 4 rounds of meta-synchronous nuclear divisions at the embryo cortex, followed by cellularization to form the cellular blastoderm. Live imaging these processes at elevated temperature revealed an increase in mitotic failures and a loss of cortical nuclei, both, during syncytial- and cellular-blastoderm stage. Additionally, embryos developing at elevated temperature show a local crowding of nuclei and an increase in asynchrony between the nuclear cycles in the middle vs. anterior/posterior poles. Interestingly, nuclear crowding and nuclear cycle asynchrony cooperatively amplify the frequency of mitotic failures, leading to holes in the blastoderm epithelium. Strikingly, the same treatment also increased embryonic lethality. We propose that the loss of nuclei results in a loss of patterning information and the abrogation of proper embryonic development. We identified genes that regulate mitosis, especially the ones mediating the interaction between microtubules and F-actin, and functionally tested their capacity to rescue the embryonic lethality.

Our results expose a vulnerability at elevated temperatures in the interaction between cortical actin and microtubules, which leads to mitotic failures, and can be potentially rescued by modulating the expression of just a few factors. We propose that the expression levels of the corresponding genes could be used as indicators to predict fitness effects on insect populations that are exposed to increasing temperature variations.

Keywords:

Syncytial blastoderm, elevated temperature, microtubule - F-actin interaction, nuclear division defects, embryo lethality, genetic rescue, *Drosophila*

Introduction:

Temperature is a key factor determining the fidelity of embryonic development. Studies have shown occurrence of birth defects due to hyperthermia during pregnancy (Edwards 2006; Miller and Church 2013; Graham 2020), in spite of active regulation of core temperature. Here, the cell biological basis for the developmental defects due to an exposure to high temperature, remains elusive. It is currently unclear whether this phenomenon could be observed and studied also in invertebrate species, for which the developmental process is well described, allowing for a quantitative characterization of the potential developmental defects arising due to high temperature. In this context, we explore whether the exposure to elevated temperature is detrimental to embryonic development in *Drosophila melanogaster* (henceforth, *Drosophila*), addressing the cell biological basis for possible defects, and asking what are the consequences in terms of population level parameters, such as embryo survival.

Previous studies have shown that the early embryonic development of *Drosophila* embryos (first ~6 hours) is especially sensitive to acute heat-shock (Welte et al. 1993), and have indicated that acute heat-shock causes a loss of coordination in developmental processes, leading to developmental defects (Crews, McCleery, and Hutson 2016). Given that the survival after a heat-shock relies on transcription of heat-shock proteins (Graziosi et al. 1980), and that zygotic transcription is progressively activated during maternal-to-zygotic transition (Pritchard and Schubiger 1996), it is likely that the developmental processes prior to the completion of this transition are especially susceptible to heat-shock. In line with these expectations, previous studies have demonstrated a disruption of the normal dynamics of cytoskeletal elements due to an exposure to high temperature (Walter, Petersen, and Biessmann 1990; Zheng et al. 2013; Figard et al. 2019). Even more elusive are the effects of prolonged exposure to elevated temperature below the heat-shock limits. Here we focus on such temperature sensitivity of early embryonic development in *Drosophila*, and ask what is the cell biological basis for developmental defects due to an exposure to elevated temperature, and whether there is a link to the population level consequences on embryo survival.

Post fertilization, the *Drosophila* embryos undergo 9 rounds of syncytial nuclear divisions deep in the yolk. Following these divisions, most nuclei migrate to embryo periphery, where 4 more rounds of nuclear division take place during a stage called, syncytial blastoderm (Foe and Alberts 1983). These nuclear divisions are facilitated by pseudo-cleavage furrows, i.e., temporary membrane invaginations resembling a half-cell that slowly form around the nuclei during interphase-metaphase, and are then rapidly reabsorbed into the embryo cortex during anaphase-telophase (Xie and Blankenship 2018). Following these 13 rounds of nuclear divisions, the resulting ~6000 nuclei simultaneously segregate into individual cells, in the process of cellularization, producing the blastoderm epithelium (Mazumdar and Mazumdar 2002). At this point gastrulation starts, which involves cell shape changes (Martin 2020), cell contact rearrangements (Lecuit and Yap 2015), and further rounds of cell divisions in isolated mitotic domains (Foe 1989): all facilitating the early morphogenesis. Cell biological basis for these early developmental processes is well described, and would allow us to identify the defects at elevated temperature, if any.

In our experiments, we exposed *Drosophila* embryos to the elevated temperature, and compared them with normal temperature controls. Following previous studies, we chose 29°C as elevated temperature (Kuntz and Eisen 2014; Chong, Amourda, and Saunders 2018) and asked whether increased temperature up to 29°C resulted in developmental defects. Notably, this temperature is well below the 32°C and higher range required to elicit a robust heat-shock response (Vazquez, Pauli, and Tissières 1993), and no major developmental defects have been reported so far at 29°C. We found that exposing embryos to elevated temperature during early embryonic development leads to a significant increase in the population level embryonic lethality. When we traced defects from the organism to the cellular level, we observed a loss of nuclei during syncytial- and cellular-blastoderm stage, which was caused by mitotic failures. Additionally, in

embryos developing at elevated temperature, we reported and quantified the nuclear crowding in the central region of the embryo, as well as greater asynchrony in the nuclear division cycles between central regions vs. anterior/posterior poles of the embryo. Moreover, we could show that the nuclear crowding and nuclear cycle asynchrony combinatorially cooperate to locally increase the propensity of mitotic failures. Such local increase in mitotic failures results in holes in the blastoderm, i.e., region devoid of nuclei/cells, to disrupt the continuity of this primary epithelial tissue. We overexpressed a few candidate genes to boost the robustness of nuclear divisions to rescue the mitotic failures defect, focusing on the regulators of cell polarity, microtubule- F-actin interactions, and mitotic spindle orientation, to test their ability to rescue the described defects, and ameliorate the embryo lethality at elevated temperature. Our results suggest a vulnerability in microtubule- F-actin interaction during the well conserved process of nuclear division, when occurring at elevated temperature. Our work establishes a novel link between cell biological defects due to an exposure to elevated temperature, and a reduction in organismal fitness at population level at elevated temperature.

Results:

Early exposure to elevated temperature reduces embryo survival.

To test whether elevated temperature had an effect on developmental robustness during the first hours of embryonic development, we exposed young embryos to 29°C and asked whether this would alter the fraction of embryos that hatch into larvae. To associate possible fitness effects with defined developmental windows (see above), embryos were exposed to elevated temperature either from deposition till before the onset of gastrulation (~3 hours) or for a duration of ~3 hours from the onset of gastrulation (Figure 1A), to keep the temperature exposures comparable. In both cases we observed a significant increase in embryonic lethality (Figure 1B). Our findings reveal a particular vulnerability during the syncytial phase of the embryonic development and suggest that elevated temperature leads to defects in the setup of the insect blastoderm. This result is surprising, especially because previous studies indicated that genetic patterning and setting up of positional information within the blastoderm was overall robust against temperature fluctuations (Lucchetta et al. 2005; Niemuth and Wolf 1995).

In addition to genetic patterning, nuclear dynamics could be challenged during the first hours of embryonic development. In this developmental window, nuclei divide deep in the yolk, then translocate to the embryo cortex, where they need to be anchored robustly while undergoing further rounds of nuclear division. A normal distribution of nuclei ultimately determines a normal morphogenesis of the blastoderm epithelium, setting the foundation for the developmental processes to follow. Thus, to address whether defects in the blastoderm could stem from defects in nuclear dynamics, we followed nuclear dynamics till the end of blastoderm formation using Histone-RFP to visualize nuclei, and Jupiter-GFP to visualize microtubules, keeping track of nuclear division cycles. Starting with nuclear migration from the yolk to periphery (occurring during the interphase of the 10th nuclear cycle), we observed nuclei through their peripheral divisions during syncytial blastoderm (through mitoses 10 to 13), and then through cellularization (interphase 14), until the onset of gastrulation could be inferred from the movement and division of nuclei (beyond interphase 14). During this time window, we did not observe any significant defects, in the nuclear translocation from deep inside the yolk to embryo cortex, in embryos developing at elevated temperature. However during the syncytial blastoderm stage, embryos that developed at 29°C much more frequently “lost” nuclei from their cortical layer than if they developed at 25°C, i.e., nuclei that were initially positioned within the cortical layer of the egg, appeared to get expelled, descended into the yolk, and did not become part of the embryonic blastoderm (Figure 1C-E), with a variability in the extent of the nuclear loss, producing holes in the blastoderm of a fraction of embryos (Figure S1). Further, in the embryos fixed and stained with DRAQ5, we imaged the nuclear distribution in the entire embryo volume, to observe that the loss of nuclei wasn’t symmetric in the two halves of the embryos, and albeit in the central region of the embryos, the location of

125 the nuclear loss varied across embryos (Figure S2). The embryo-to-embryo variability, both in the distribution
126 and intensity of nuclear loss argued for the possibility that these defects were self-organized rather than
127 dictated by the genetic make-up.

128 Taken together, we identified the syncytial blastoderm stage of embryo development as the most sensitive
129 window, based on the embryo lethality analysis. Additionally, the loss of nuclei during this stage indicated a
130 defect in nuclear anchorage at the embryo cortex, rather than nuclear divisions deep in the yolk, or the
131 translocation of nuclei from deep inside the yolk to the embryo cortex.

132 A closer observation of live imaged embryos revealed three striking phenomena during blastoderm formation
133 in embryos developing at elevated temperature compared to normal temperature controls: an extensive loss
134 of nuclei from the egg cortex (as above), a time shift and slowdown of nuclear divisions cycles in the central
135 region of the embryo compared to its poles, and nuclear crowding in the central region of the embryo. Thus,
136 we decided to quantitatively describe these defects, in an attempt to describe the necessary conditions to
137 produce a blastoderm hole, and link these defects to the embryo lethality phenotype.

138 **At elevated temperature, embryos lose nuclei from the cortex after defective divisions.**
139 A closer look at the loss of cortical nuclei indicated that the nuclei were lost either individually or as pairs of
140 two adjacent nuclei. We could also observe periods of drastic displacement of nuclei at elevated temperature
141 (see below). Based on these observations, we imagined various mechanisms for the observed loss of nuclei.
142 For instance, individual nuclei might be lost due to out-of-plane nuclear divisions, while a pair of nuclei might
143 be lost due to a defective in-plane nuclear division. In case of defects in nuclear divisions, it is possible that
144 the cell cycle checkpoints are triggered. Nuclei being dislodged from the embryo cortex during the drastic
145 displacements could also explain both individual and pairwise loss, though in such scenario, the pairs of nuclei
146 need to be somehow associated with each other, influencing each other's loss. Here we considered these
147 possibilities, and asked to what extent they account for the observed loss of nuclei.

148 To address whether cortical nuclei appeared as getting lost because of an increased frequency of out-of-
149 plane divisions, we visually tracked nuclei from their last division to the time they were no longer associated
150 with the cortex. We could detect out-of-plane divisions in embryos at temperatures ranging from 22 to 29°C,
151 only during the mitoses of the 10th nuclear cycle. These out-of-plane divisions could be easily identified, as
152 they formed a characteristic mitotic spindle that was oriented perpendicular to the embryo surface (Figure
153 S3A, B), and after the division only one of the daughter nuclei remained attached to the cortex. However, the
154 overall frequency of out-of-plane divisions was very low (<5%): neither did it differ significantly between any
155 of the observed temperatures (Figure S3C), nor could it explain the loss of nuclei during later nuclear cycles.
156 Similarly, losses of individual nuclei after an in-plane division were rather infrequent, and did not differ
157 significantly within the range of observed temperatures (Figure S3D, E). This suggested that the increased
158 loss of nuclei observed in embryos developing at 29°C could neither be accounted for with individual nuclei
159 dropping into the yolk, irrespective of whether the loss was due to them being mechanically dislodged.

160 For the observed pairwise loss of nuclei, our tracking revealed that these were sister nuclei born from the
161 same mitosis. This suggested that specific characteristics of cortical nuclear divisions might determine the
162 future fate of the newborn nuclei and trigger their release from the egg cortex, possibly in response to failed
163 checkpoints during mitosis. In the pairwise loss of nuclei, we observed chromosome segregation defects
164 (Figure 1F) that could lead to aneuploidy, suggesting that the subsequent expulsion of daughter nuclei from
165 the egg cortex was due to a prior defective mitosis. Following defective mitoses at normal or elevated
166 temperature, we could not detect a clear time course of nuclear expulsion: these nuclei could be lost in the
167 immediately following or in later interphases (Figure S4), suggesting that nuclear expulsion after defective
168 mitosis was a passive process and not triggered by molecular signaling at failed checkpoints.

169 To confirm that the observed loss of nuclei at 29°C could be attributed to an overall increase in defective
170 mitoses, we asked if the frequency of defective mitoses was changing depending on the temperature. To
171 address this question, we focused on interphase 14, as that's when we observed the most nuclear losses,
172 and counted the pairwise loss of nuclei after mitotic failures at 22, 25, 28, and 29°C (see methods). While the
173 frequency of mitotic failures was overall low at 22 to 28°C, it increased significantly at 29°C (Figure 1G). Taken
174 together, our findings identify nuclear divisions in the blastoderm as a thermolabile cellular process (Figure
175 1H) that shows a disproportionate increase in failures at the transition from 28°C to 29°C, resulting in the loss
176 of sister nuclei from the egg cortex, when born in defective mitoses. Interestingly, in a fraction of embryos
177 the mitotic failures occurred in great numbers and in close vicinity, leading to the holes in the blastoderm
178 epithelium (Figure 1G, hollow markers). Thus, the formation of blastoderm holes (Figure S1) could be directly
179 attributed to clustered mitotic failures, though it remained unclear why some embryos have the of mitotic
180 failures in local clusters, while others didn't.

181 To explore the potential cause of mitotic failures at elevated temperatures, we tracked nuclear clusters
182 starting from individual mother nucleus (end of interphase 10) to the 8 great-granddaughter nuclei (end of
183 interphase 13), in order to quantitatively describe their movement (Figure S5A-C, also see methods). This
184 allowed us to assess mechanical stresses that would be experienced by nuclei dividing at the blastoderm
185 cortex, as we distinguished the movement of nuclear clusters during interphase-metaphase vs. anaphase-
186 telophase. Our results showed that the nuclear clusters had 2 components to their movement. First, the
187 clusters exhibited a constant drift-like movement, which we captured using a linear fit to the displacement
188 of the center of the nuclear clusters over time (Figure S5B dotted lines). The slope of the linear fit indicated
189 that the clusters drifted towards the posterior end (Figure S5D, E). The second component was composed of
190 deviations in the centers of nuclear cluster from the linear fit, i.e., the displacements relative to the first
191 component. These deviations were significantly greater at elevated temperature, both during the interphase-
192 metaphase period (Figure S5F, G) and during the anaphase-telophase period (Figure S5H, I), though the
193 displacements along AP-axis were more drastic than those along DV-axis, and those during anaphase-
194 telophase were 2-3-fold greater than those during interphase-metaphase. For context, the length scale of
195 the displacements during anaphase-telophase could be up to 4-times the length of the spindle itself,
196 indicating an extensive propensity for displacement in x-y plane, especially along the AP axis. We also
197 observed that the spindles were getting displaced in z-axis, again, during anaphase-telophase period. In
198 embryos developing at 29°C, we could see two waves of nuclear displacement, originating from the anterior
199 and the posterior pole, meeting at the central region of the embryo (Figure S6). Overall, these quantifications
200 and observations indicated that the mitotic spindles are displaced drastically while nuclei are dividing, and
201 argued for the possibility of mechanical defects during nuclear divisions.

202 Taken together, we observed the effects of exposure to elevated temperature, at organismal level as embryo
203 lethality (Figure 1B), at tissue level as blastoderm holes (Figure 1E, Figure S1, S2), and at cellular level as
204 mitotic failures (Figure 1F, G). Embryos with most severe form of mitotic failure phenotype had blastoderm
205 hole, while the fraction of embryos with large blastoderm holes correlated well with increase in embryo
206 lethality, indicting a link from cellular till organismal phenotype. Given that the loss of nuclei occurs after
207 mitosis, and that the nuclei move drastically during anaphase-telophase period, we further argue that nuclear
208 anchorage is specifically challenged during mitosis.

209 **Nuclei divide with a time shift and are crowded in embryos at elevated temperature.**
210 The most severe loss of nuclei was often observed in the central domain of the embryo (Figure 1C-E, Figure
211 S1 and S2). Notably, these areas coincided with the "collision" of two waves of nuclear displacements along
212 z-axis (Figure S6), i.e., the future apical-basal axis in the blastoderm cells (A. Schmidt and Grosshans 2018).
213 We could further observe that, not only anaphase, but all other phases of nuclear division were delayed in

214 the central region of the embryos developing at 29°C. This resulted in regions of embryo being segregated
215 into domains of nuclear division phases (Figure 2A). Conversely, the same phase of nuclear division cycle
216 could be observed at different timepoints in different regions of the embryo (Figure S7). Thus, we decided to
217 quantify this asynchrony of nuclear division cycles as a function of temperature (see methods). Our
218 quantifications show that the asynchrony significantly increases in embryos developing at 29°C as compared
219 to other temperatures (Figure 2B). Thus, we quantitatively describe the defect of asynchrony in nuclear cycles
220 at elevated temperature (Figure 2C).

221 The central region of the embryo, which corresponded to the delayed nuclear division cycles, also had more
222 tightly packed nuclei. To quantify nuclear crowding, we focused on the last nuclear division cycle and its
223 preceding interphase, i.e., interphase 13 (see methods), as that's the time we observed maximum nuclear
224 crowding. To quantify the space available for cortical blastoderm nuclei, we segmented the nuclei, and used
225 Voronoi tessellation to define a region around each nucleus, which we call pseudo-cells. The areas of pseudo-
226 cells were rather homogeneous in embryos developing at 22°C (Figure 2D, H, L). Already at 25°C (Figure 2E,
227 I, M) and 28°C (Figure 2F, J, n), the available space for cortical nuclei was no longer uniform across the
228 embryo, and it showed signs of local crowding. At 29°C, the space available for nuclei along the anterior-
229 posterior axis varied substantially and revealed strong nuclear crowding in the central region of the embryo
230 (Figure 2G, K, O). We quantified the extent of crowding (see methods) as a function of temperature, and
231 found a progressive increase in the nuclear crowding (Figure 2P). Thus, we also quantitatively describe the
232 defect of nuclear crowding at elevated temperature (Figure 2Q).

233 Taken together, besides mitotic failure, we have two additional defects at elevated temperature, nuclear
234 crowding and nuclear cycle asynchrony. We also note that the severity of these defects (based on the
235 quantifications) can vary between embryos, e.g., the embryos with most extensive failure in mitosis
236 (blastoderm holes) don't have the highest levels of nuclear crowding (Figure 2P), or strongest asynchrony
237 (Figure 2B), etc. Though, based on the quantifications and statistical significances we note that; one, severe
238 mitotic failures (blastoderm holes) appear in a threshold-effect-like manner, appearing only in a fraction of
239 embryos at 29°C; two, the nuclear crowding and asynchrony in nuclear cycles appears progressively as
240 function of temperature, although the progression is not linear; and three, the fraction of embryos with large
241 blastoderm holes best explains the increase in embryo lethality. Thus, we hypothesize a hierarchy of the
242 defects, purely based on the fraction of embryos in which they appear as a function of temperature: exposure
243 to elevated temperature will increase the frequency of mitotic failures as primary defect; nuclear crowding
244 and nuclear cycle asynchrony will secondarily dictate the distribution of mitotic failures, producing extensive
245 mitotic failures (blastoderm holes) as the ultimate effect in a fraction of embryos; eventually leading to a
246 reduction in embryo fitness and an increase in embryo lethality.

247 **Regions of embryo with greater nuclear crowding and with delayed nuclear cycles are associated with**
248 **greater frequency of mitotic failures.**

249 To test whether nuclear crowding and nuclear cycle asynchrony could influence the propensity of mitotic
250 failures, we decided to compute the fraction of mitotic failures occurring in the regions of the embryo that
251 had nuclear crowding and/or delayed nuclear division cycles. We constructed regions of the embryo with
252 maximum nuclear crowding (crowded regions), maximum delay in nuclear division cycles (delayed regions),
253 and using an overlap of crowded and delayed regions (combined region) (see methods).

254 We defined the crowded regions (Figure 3A), and delayed regions (Figure 3B) based of the distribution and
255 dynamics of nuclei in live imaged embryos. Then, we overlayed the map of mitotic failures on the crowded
256 regions (Figure 3C), delayed regions (Figure 3D), and the combined regions (Figure 3E). The crowded and
257 delayed regions had rather comparable areas across temperatures (Figure 3F, G), indicating that any

258 difference in the fraction of mitotic defects would be solely due to the nuclear crowding or due to the delays
259 in nuclear cycles. Interestingly, the areas of the combined regions were smaller at elevated temperature
260 (Figure 3H), indicating that there was an increase in the overlap between the crowded and delayed regions,
261 and that we should expect a similar reduction in the fraction of mitotic failures, if the mitotic failures were
262 distributed randomly.

263 The fraction of mitotic failures in crowded region increased progressively as function of temperature,
264 reaching statistical significance for comparison between 22 and 29°C (Figure 3I), while the fraction of mitotic
265 failures in delayed regions did not increase progressively, showing an abrupt increase from 28 to 29°C with
266 only marginal statistical significance (Figure 3J). Interestingly, we see that the smaller area fractions in the
267 combined regions correspond to even greater fraction of mitotic failures (Figure 3K). Additionally, the
268 distribution of the fraction of mitotic failures in the combined region was unimodal, in contrast to the bimodal
269 distribution of mitotic failures themselves (Figure 1G). Thus, we conclude that the combinatorial effect of
270 nuclear crowding and asynchrony significantly increases the propensity of mitotic failures. We would further
271 argue that nuclear crowding has a stronger impact on the propensity of mitotic failures than that due to
272 nuclear cycle asynchrony.

273 Taken together, we find large clusters of defective mitoses and subsequent loss of nuclei in the center of
274 about 10-20% of embryos developing at 29°C (Figure 1G). Nuclear crowding and nuclear cycle asynchrony
275 cooperate to produce "hot spots" of mitotic failures (Figure 3). The aggregated losses of nuclei in the center
276 of the embryo persist until the end of blastoderm formation and leads to visible holes in the newly formed
277 embryonic epithelium (Figure S1). These holes indicate a severe disruption in epithelial integrity and
278 approximately match the increased rate of embryonic lethality for development at 29°C (Figure 1B). Going
279 further, we attempted to rescue the embryo lethality defect using over-expression of various candidate
280 genes, and if a rescue was possible, further decided to quantify whether the rescue could be explained
281 through fraction of mitotic failures in the crowded region and the combined region.

282 **Identifying temperature-sensitive vulnerabilities in a deeply conserved cellular process**

283 The analysis of early fly development at moderately elevated temperatures, in our experiments, has
284 uncovered the first three hours of fly development as sensitive to environmental perturbations, which can
285 affect embryo fitness and increase embryonic lethality at elevated temperatures. This increase in embryonic
286 lethality correlates with specific perturbations in fundamental nuclear dynamics, i.e., the timing and fidelity
287 of nuclear divisions within the spatial constraints of a cortex densely packed with nuclei. To address how a
288 deeply conserved and presumably robust process like mitosis could be affected so dramatically at a
289 temperature lower than those eliciting a heat-shock response, we functionally probed for possible
290 vulnerabilities in core molecular interactions that control nuclear dynamics in the early fly embryo.

291 In stark deviation from canonical cytokinesis, cortical nuclear divisions in the syncytial fly embryo rely on cell
292 polarity cues that are set up at shallow metaphase furrows of the egg cortex, where they orient mitotic
293 spindles parallel to the cell surface (A. Schmidt and Grosshans 2018; Xie and Blankenship 2018). What's more,
294 these furrows are transient, and are reestablished during each nuclear cycle: including new growth of
295 membrane between nuclei, reestablishment of cell polarity, and reorganization of cytoskeletal elements. The
296 dependence on transient membrane invaginations to establish cell polarity information represents the least
297 conserved and potentially most labile element of cortical nuclear divisions in insect embryos. To test whether
298 the fidelity of cortical mitoses at elevated temperatures hinges upon insufficiently robust cell polarity
299 signaling, we overexpressed two known prominent polarity proteins, Bazooka (baz, a Par-3 homolog) and
300 Disks-large (dlg) (Harris and Peifer 2004). We asked whether these over-expressions rescue embryo lethality

301 defect, and if so, whether the increase in the fraction of mitotic failures in crowded regions and in combined
302 regions is rescued as well.

303 When we over-expressed either *baz* or *dlg* we did not see a significant change in embryo lethality at control
304 temperature (25°C) as compared to the control (Figure 4A). The lethality was greater in outcross controls at
305 elevated temperature (29°C) similar to results in previous experiments (Figure 1B), while the embryos over-
306 expressing either *baz* or *dlg* faired significantly better at the elevated temperature (Figure 4A). We note
307 however that the rescue of lethality at elevated temperature in *baz* over-expressing embryos was only
308 marginally significant, with a lot of variability between samples. Additionally, *dlg* over-expressing embryos at
309 normal temperature showed higher variability in embryo lethality than their outcross control counterparts.
310 Consistent with these results, *baz* over-expression did not rescue the increase in the fraction of mitotic
311 failures, either in the crowded regions, or in the combined regions at elevated temperature (Figure 4B, C),
312 though the large blastoderm holes were absent in these embryos. Then, *dlg* over-expression rescued the
313 increase in fraction of mitotic failures only in the crowded region at elevated temperature (Figure 4B, C), and
314 while the large blastoderm holes were absent in these embryos, *dlg* over-expression increased the fraction
315 of mitotic defects at normal temperature in both, the crowded region and in the combined region,
316 occasionally producing small blastoderm holes (Figure 4B, C).

317 Above results indicated a temperature-dependent vulnerability more specific to the molecular core of the
318 mitotic spindle rather than its setup in the context of a syncytial embryo. To faithfully pull sister chromatids
319 towards the actin cortex on either side of the division plane, the execution of mitosis relies on tightly
320 regulated interactions between the actin cortex and the microtubules of the mitotic spindle (Cao et al. 2010;
321 Rizzelli et al. 2020). In *Drosophila*, these critical interactions of actin and microtubules have been associated
322 with a complex of three proteins: α-Catenin (αCat), which binds to the actin cortex; β-Catenin (βCat, or
323 armadillo in Drosophila), which binds to α-Catenin; and Adenomatous polyposis coli 2 (Apc2), which links to
324 βCat and binds to the microtubules of the mitotic spindle (McCartney et al. 2001). Within this tripartite
325 complex, the interaction of αCat and βCat is direct, and is presumably not regulated, whereas the interaction
326 of βCat and Apc2 is mediated by a specific kinase, the Drosophila homolog of the Glycogen Synthase Kinase
327 3β, Shaggy (sgg) (Rim, Clevers, and Nusse 2022). Additional indication for the activity of the complex came
328 when we fixed and stained embryos developing at elevated temperature, to visualize nuclei and cortical F-
329 actin (see methods). We could observe F-actin structures in embryos at elevated temperature (Figure S9, see
330 panel F), which were reminiscent of those in embryos mutant for *Apc2*, β*Cat*, or *sgg*, as previously described
331 (McCartney et al. 2001). Thus, we hypothesized that boosting the activity of the complex through over-
332 expression of one or more of its components should meaningfully rescue the embryo lethality defect, and
333 the increase in the fraction of mitotic failures in crowded regions and in combined regions.

334 To test whether the fidelity of cortical mitoses at elevated temperatures was affected by insufficiently tight
335 or poorly controlled coupling of actin and microtubules, we overexpressed either *αCat* or *sgg*, and again
336 asked whether the increase in embryo lethality at elevated temperature was rescued. When we over-
337 expressed either *αCat* or *sgg* we did not see a significant change in embryo lethality at control temperature
338 (25°C) as compared to the control (Figure 4D). The lethality was greater in outcross controls at elevated
339 temperature (29°C) similar to results in previous experiments (Figure 1B, Figure 4A), while the embryos over-
340 expressing either *αCat* or *sgg* faired significantly better at the elevated temperature (Figure 4D). Consistent
341 with these results, both *αCat* and *sgg* over-expressions rescued the increase in the fraction of mitotic failures,
342 in the crowded regions, as well as in the combined regions at elevated temperature (Figure 4E, F), with the
343 large blastoderm holes absent in these embryos. These results suggested that an experimental strengthening
344 of actin binding was able to attenuate temperature-dependent destabilizations of the mitotic spindle. These

345 findings are consistent with the idea that the scaffolding activity of αCat, βCat, and Apc2, mediated by sgg,
346 constitutes a thermosensitive controller of nuclear division fidelity in the early blastoderm embryo.

347 Given the reduction in mitotic fidelity at elevated temperature, we were wondering whether any regulator
348 of mitosis could rescue temperature defects upon overexpression. To test this possibility, we tested other
349 regulators of mitosis and focused on the activity of mud and insc. In epithelia, the activity of 'Mushroom body
350 defect' (mud, NuMA homolog) and that of Inscuteable (insc) is known to dictate the orientation of mitotic
351 spindle during cell division (Mapelli and Gonzalez 2012). Similar activity might be present for nuclear divisions
352 during syncytial blastoderm stage, raising the possibility that over-expression of *mud* or *insc* could rescue
353 embryo lethality, presumably through reducing mitotic failures. However, neither of the over-expressions
354 ameliorated the increased embryo lethality at elevated temperature, with mud over-expression additionally
355 increasing the lethality at normal temperature as well (Figure S11). This failure to rescue embryo lethality
356 further allowed us to argue that, the elevated temperature critically challenges the core machinery of mitotic
357 spindle, more so than the regulation of spindle orientation.

358 **The natural distribution of a few regulators of spindle dynamics varies along thermoclines.**
359 Our analyses showed how elevated temperatures during the first hours of fly development affect early
360 embryonic cell biology; it may seem suggestive, but it was not shown that naturally occurring changes similar
361 to our overexpression of cytoskeletal regulators could shape the evolution of fly or insect development in
362 general. To address this possibility more directly, we analyzed the distribution of standing genetic variations
363 associated with the regulation of the spindle dynamics (combination of GO terms, cell polarity, spindle
364 organization, and spindle localization), and tested the hypothesis that such variation was randomly
365 distributed with respect to described thermoclines (continent-scale gradients of annual mean temperature).
366 We found that indeed, most standing genetic variation associated with putative spindle dynamics regulators
367 was distributed without a clear thermoclinal pattern, although the fraction of genes showing clinal
368 distribution was greater than those associated with a more generic GO term like 'metabolic process' (Figure
369 4G, Table S1). A clear and notable outlier in this analysis was *sgg*, which was marked with a north/south clinal
370 distribution of natural variations independently in populations in the US, in Europe, and in Australia (see also,
371 Table S2). These findings strongly suggest that the thermosensitivity that *sgg* exhibits in lab conditions,
372 constitutes a biological property that can be exposed and selected for also in natural populations and during
373 the course of evolution. Similarly, we found that 'scribble', a cell polarity protein which interacts with dlg
374 (Khoury and Bilder 2020; 2022), was also clinal in all 3 populations. Further experiments are required to
375 formally test the possibility of a rescue of embryo lethality with over-expression of *scribble*, which will be
376 addressed in future experiments.

377 **Discussion:**

378 **Cellular basis of the sensitivity against elevated temperature during early embryonic development**
379 With our work, we demonstrate how the first hours of embryonic development are vulnerable to an exposure
380 to temperatures below the heat-shock range. We identify the mechanistic basis for this vulnerability: the
381 thermolability of the interaction between microtubules and F-actin during mitosis. Given that these early
382 processes till blastoderm formation are conserved across insects (Lynch, El-Sherif, and Brown 2012; Lemke,
383 Kale, and Urbansky 2020), our results implicate a vulnerability in a plethora of insect species. It would be
384 interesting to investigate whether mechanisms exist in nature to accommodate for this vulnerability. In the
385 backdrop of this sensitivity, it is the challenge for the embryo to establish an egg cortex that is uniformly
386 populated with cortically anchored nuclei that carry positional information for subsequent steps of epithelial
387 morphogenesis and cell differentiation. A defect in these early morphogenetic processes and cell
388 differentiation could lead to defects in subsequent processes, ultimately leading to developmental failure

389 and embryo lethality. Thus, with our data, a mechanism emerges to establish the link between the proximate
390 effects of elevated temperature on cytoskeletal regulation during mitosis, and its ultimate impact on the
391 survival of embryos.

392 What is the best predictor of lethality in embryos exposed to elevated temperatures? In our analysis, we
393 found three defects in embryos at elevated temperature: mitotic failures, nuclear crowding, and nuclear cycle
394 asynchrony. Mitotic failures, especially during the last mitosis prior to cellularization, can lead to loss of
395 nuclei, and consequently a loss of local positional information that is advected and lost with the nuclei. This
396 can lead to missing cell fates in the coordinate system of the embryo, leading to missing embryonic
397 structures, which can pose challenges for developmental fidelity. Comparing the fraction of dead embryos at
398 elevated temperature vs. the severity of mitotic failures, we would argue that the embryos with the most
399 severe mitotic failures, i.e., those that end up with holes in blastoderm epithelium, are the ones that don't
400 hatch into larvae. In our over-expression conditions, it is clear that the severe mitotic failures (blastoderm
401 holes) are absent in the genotypes that rescue the embryo lethality at elevated temperature. It remains to
402 be seen whether an extensive, but scattered, loss of nuclei poses any developmental disadvantage to the
403 embryo. It is possible that such disadvantages might be apparent only during larval stage, and might directly
404 affect larval fitness, but our current analysis wouldn't capture that effect. Additionally, developmental
405 robustness can vary between species, which raises the possibility that not all fly species will be able to
406 accommodate such developmental disadvantages. Further, here we have presented 28 embryos of control
407 genotype at elevated temperature, of which 6 have large- and 5 have small blastoderm holes. In all of these
408 cases, the blastoderm holes appear in the region where we see an overlap between nuclear crowding and
409 the delay of nuclear divisions. We further argue that the severe version of the defect at elevated temperature
410 (blastoderm holes) occur where the three phenomena (mitotic failures, nuclear cycle asynchrony, and
411 nuclear crowding) spatially overlap, further supported with our quantifications of fraction of mitotic failures
412 in combined regions. Thus, even though all of the 3 defects can independently reduce embryo fitness, we
413 demonstrate that the defects cooperate, to induce lethality in a fraction of embryos.

414 **Genetically increasing robustness of early embryos against environmental perturbations**

415 In theory, the robustness of embryonic development can be higher depending on, say, the quality of the food
416 available to the mother. Thus, one can hypothesize a rescue of embryonic lethality at elevated temperature
417 through, e.g., improvement of the quality of the diet available to the adult females. A previous study
418 compared the effect of temperature and the atmospheric O_2 levels on embryo survival, where they report
419 consistently greater embryo survival at 25% Oxygen concentration, than the normal 21% (Kuntz and Eisen
420 2015). These results indicate that it might also be possible to increase the robustness of embryo development
421 through increasing the atmospheric O_2 concentration. However, such solution might not be heritable, and
422 might not confer an increase in future fitness. Previous studies have increased embryo survival in face of
423 exposure to elevated temperature through over-expression of heat-shock proteins (Lockwood, Julick, and
424 Montooth 2017). Presumably, this increases the capacitance of the system to tolerate environmental insults,
425 akin to how heat-shock proteins are known to act as capacitors for genetic variation (Rutherford and
426 Lindquist 1998; Sangster, Lindquist, and Queitsch 2004). However, such a rescue would not shed light on
427 underlying biology of temperature defects, as the effect of such perturbations on the mitotic failures would
428 remain nebulous. Thus, to rescue the lethality at elevated temperature, we used our cellular level
429 understanding of the defects to guide our choice of candidate genes for genetic manipulations. This approach
430 additionally allowed us to challenge our cellular level understanding of the defects at elevated temperature,
431 as we construct and test hypotheses about the over-expression of various genes towards a genetic rescue.

432 Various genotypes in our experiments, specifically the overexpression of *αCat*, *sgg*, *baz*, or *dlg*, either rescue
433 or reduce the severity of one or more defects (embryo lethality, presence of blastoderm holes, fraction of

434 mitotic failure in crowded region, or that in the combined region) that occur due to an exposure to elevated
435 temperature. Here, we would argue that *αCat* and *sgg* overexpression are the superior experimental
436 condition among these as far as potential for a rescue is concerned, as they produce virtually no side-effects
437 (unlike *dlg* overexpression at normal temperature), while robustly reducing the lethality at elevated
438 temperature (unlike *baz* overexpression). Additional support for this notion comes from our analysis of the
439 presence of natural variation along thermoclines, where we identified *sgg* as an interesting candidate gene,
440 along with *scribble*. The list of genes associated with spindle dynamics (combination of GO terms spindle
441 organization, spindle localization, and cell polarity) included our candidate genes *baz*, *dlg*, *sgg*, *mud*, and *insc*.
442 While *αCat* is not presently associated with GO terms related to spindle dynamics, we also did not find it to
443 be clinal in our extensive literature search. It is possible that natural fly populations don't possess sufficient
444 standing genetic variation at that locus that could provide a selective advantage. In any case, an overlap
445 between our candidates and potential natural candidate genes increases our confidence in our approach to
446 mitigate the detrimental effects of an exposure to elevated temperature during early embryonic
447 development.

448 Given that both *αCat* and *sgg* overexpression show a robust rescue of embryo lethality, we would further
449 argue that the interaction between microtubules and cortical F-actin, as supported by the tripartite protein
450 complex between αCat, βCat, and Apc2, mediate by sgg, is sensitive to temperature fluctuations. It is likely
451 that the association/dissociation constants decrease/increase for one or more binding interactions (F-actin
452 with αCat, αCat with βCat, and βCat with Apc2) as the temperature increases. It is also likely that the kinase
453 activity of sgg reduces with an increase in temperature, hampering the association between βCat and Apc2.
454 Further experiments are required to test these ideas. However, here we also note that many nuclei manage
455 to divide in embryos mutant for βCat, Apc2, and sgg (McCartney et al. 2001), forming a somewhat defective
456 blastoderm. This would indicate presence of alternative mechanisms that can also be reinforced to increase
457 the robustness of mitosis, and identifying and testing such mechanisms would be of great interest to rescue
458 embryo lethality at elevated temperature.

459 **How fast can nature increase the robustness against the adverse effects of elevated temperature?**
460 In a recent study (Rudman et al. 2022), the researchers allowed fly populations to naturally evolve from spring
461 through summer till the fall season, and found that specific single nucleotide polymorphisms were selected
462 for in the regulatory regions of *sgg* and β*Cat*, along with many other genes. This further indicates that nature
463 might be exploiting the allelic plasticity in our candidate genes at rather rapid timescales of just a few
464 generations, to increase robustness against elevated temperatures. It is interesting to see that these genes
465 show selectable variation at the population level, and that an over-expression of *sgg* in our analysis is capable
466 of rescuing the embryo lethality at elevated temperature. To be clear, the study does not comment on
467 whether the accumulated mutations lead to an over-expression or hyperactivation of *sgg*, and at which stage
468 during the life cycle. At the same time, the analysis won't pick up candidates that don't have sufficient
469 variation in the seed population. In any case, our functional analysis can be effectively used to test for the
470 function of any gene that rescues (or worsens) the effect of elevated temperature on early embryonic
471 development, in any fly embryo that's amenable to experimental manipulations. We believe that our
472 experimental pipeline holds the promise to uncover exciting biology, while understanding how physiological
473 processes are affected by the exposure to elevated temperature.

474 **Sensitivity of early embryonic development to the global warming and climate change**
475 Climate change is a global problem that threatens the existence of life on earth as we know it (IPBES 2019).
476 In this context, we decided to focus on effect of elevated temperature on the physiology of flies, given their
477 vital roles for the functioning of ecosystems (Raguso 2020). We found the early embryonic development in
478 *Drosophila* to be especially sensitive to an exposure to elevated temperature. Here, we identified the

syncytial blastoderm stage during embryonic development as the earliest possible time window that's sensitive to elevated temperature. We could also observe cascading defects in the cellular blastoderm formed thereafter. An increase in embryonic lethality, due to the early exposure to elevated temperatures, further indicated that, presumably, the subsequent developmental processes are affected as well. We also see a small increase in embryonic lethality when we expose post-cellularization embryos to elevated temperature, indicating additionally that the temperature sensitive time window might actually be longer than just the pre-gastrulation developmental phase. It is easy to imagine that, in wild, embryos would be exposed to elevated temperature for first few hours, starting from egg lay till well beyond gastrulation. Given that these early processes during the embryonic development are conserved across fly species (Lemke, Kale, and Urbansky 2020), our results raise the possibility that many other key species, would exhibit similar defects during early embryonic development, will have an increase in lethality, and will be overall threatened due to global warming. It is rather impressive that an exposure to a sub-heat-shock elevated temperature during first few hours of embryonic development is capable of reducing the fitness of the entire embryonic development to increase embryonic lethality: an effect which is presumably conserved across the animal kingdom, and would be worth exploring at the cellular level to improve embryo survival. Perhaps, the temperature sensitive developmental window is so crucial as it includes gastrulation, very much in agreement with the famous quote from Lewis Wolpert, "It is not birth, marriage, or death, but gastrulation which is truly the most important time in your life".

498 **Materials and methods:**

499 Fly lines and genetics:

500 *OregonR* line was used as WT *Drosophila*.

501 *Histone-RFP* expresses RFP tagged version of His2Av. Insertion on 3rd chromosome. Bloomington Drosophila
502 Stock Center (BDSC) #23650.

503 *Jupiter-GFP* expresses GFP tagged version of microtubule binding protein Jupiter. Insertion on 3rd
504 chromosome. Always used in combination with *Histone-RFP*. Gift from Jan Felix Evers.

505 *67-Gal4* (mat αTub-GAL4-VP16) is a maternal specific Gal4 driver. Insertion on 2nd chromosome. Always used
506 in combination with *Histone-RFP* and *Jupiter-GFP* in the over-expression experiments (see below). Gift from
507 Thomas Lecuit.

508 The following lines were used to drive the over-expression of various genes of interest in an attempt to rescue
509 the effects of elevated temperature. *baz*, BDSC #17613; *dlg*, BDSC #15779; *αCat*, BDSC #65590; *sgg*, BDSC
510 #15886; *mud*, BDSC #22371; *insc*, BDSC #39676. An outcross to *w1118* was used as control.

511 For various over-expression experiments, we first crossed virgins from the Gal4 line '+; 67-Gal4; Jupiter-GFP,
512 Histone-RFP' to the males of over-expression line 'UAS-X; +; +' (X= *baz*, *dlg*, *sgg*, or *mud*) or '+; +; UAS-Z' (Z=
513 *αCat*, or *insc*), or to males of *w1118* as control. F1 virgin females from these crosses were back crossed to
514 males of the same paternal genotype.

515 Genotypes associated with various figure panels are listed in Table S3.

516 Embryo collection: For any experiment, we put males and females of appropriate genotypes (Table S3) into
517 transparent cylindrical embryo collection cages (inner diameter ~5 cm). Fine wire mesh is glued to top side
518 of the cage to allow air exchange while keeping the flies trapped, and the bottom of the cage is closed with
519 apple-juice agar plates bearing a thin layer of yeast paste, where flies deposited the embryos. To prepare the
520 agar plates, we typically prepare 1 l of apple-juice agar solution. For this, we boiled 24 gm of agar in 750 ml
521 of water, to which we added 250 ml of fresh store-bought apple juice, while stirring on a hot plate. We make
522 the final amount of sucrose to 25 gm: the amount of additional sucrose depends on the sugar content of the
523 apple juice. This solution is sufficient for ~80 petri-dishes of 6 cm diameter. After agar is solidified, the plates
524 can be stored for long time at 4°C. Before the embryo collection, the plates were covered with a thin layer of
525 yeast paste (to stimulate oviposition), and were pre-incubated to the embryo collection temperature
526 depending on the temperature regimen, for at least half an hour. *Drosophila* females are known to hold onto
527 the embryo long after fertilization, such that a large part of the early embryo development can occur inside
528 the abdomen. To avoid these embryos, we perform a sham embryo collection for about an hour at room
529 temperature (24-25°C), from which all embryos are discarded. Following this sham collection, we collect the
530 embryos that are actually used in the experiment at the specific experimental temperature.

531 Embryo lethality experiment: There were 3 temperature regimes in the embryo lethality experiments, as
532 depicted in Figure 1A. Depending on the regimen, we collected embryos for 1 hour either at normal
533 temperature (24-25°C) or elevated temperature (29-30°C). The 24-25°C collections (corresponding to normal
534 temperature) were done on the bench top. The 29-30°C collections (corresponding to elevated temperature)
535 were done in a water bath, where the bottom surface of the embryo collection agar plate is in thermal contact
536 with the heated water. For NN or EN, we collected embryos for 1 hour either at normal temperature or
537 elevated temperature, and then incubated them at the same temperature for another 2 hours. Afterwards,
538 the embryos are washed with bleach for 10-15 seconds, then washed thoroughly with tap water, aligned on
539 a 24x60 mm rectangular coverslip, and covered with halocarbon oil. For NE, we collected embryos for 1 hour

540 at normal temperature, and then incubated them at the same temperature for another 1.5 hours. Within the
541 next half an hour, the embryos are washed with bleach for 10-15 seconds, then washed thoroughly with tap
542 water, aligned on a 24x60 mm rectangular coverslip, and covered with halocarbon oil. Then, we incubated
543 them at elevated temperature for 3 hours. Then, for all the temperature regimen, the coverslips with
544 embryos were incubated at normal temperature for about a day, following which we counted the number of
545 eclosed larvae, and the number of dead embryos. The embryonic lethality was estimated as,

546 $$embryo\ lethality\ = \frac{100 * number\ of\ dead\ embryos}{number\ of\ dead\ embryos\ +\ number\ of\ larvae}$$

547 We excluded the unfertilized embryos from these calculations.

548 Imaging fixed embryos: We used 2 different temperature regimens for embryo collection for fixation and
549 staining. We collected embryos for 3-4 hours either at normal temperature (24-25°C) or elevated
550 temperature (29-30°C). The 24-25°C collections (corresponding to 25°C regimen) were done on the bench
551 top. The 29-30°C collections (corresponding to 29°C regimen) were done in a water bath, where the bottom
552 surface of the embryo collection agar plate is in thermal contact with the heated water. Afterwards, the
553 embryos are washed with bleach for 40-45 seconds, washed thoroughly with tap water, and fixed
554 immediately. Collecting embryos for longer duration is not a problem here, as we only image and analyze the
555 embryos that are before gastrulation stage, through *post hoc* identification of developmental stage. Here,
556 we did 2 kinds of experiments; one, where the aim was visualizing the nuclei from the entire embryo (data
557 in Figure S2); and two, where the aim was visualizing the nuclei along with F-actin distributions from half
558 embryos (data in Figure S9). Accordingly, we used 2 different protocols for embryo fixation, staining,
559 mounting, and imaging.

560 To **visualize all nuclei from the entire embryo**, we used heat fixation, and stained the embryos with DRAQ5.
561 Briefly, we transferred the processed embryos to 50 ml tubes with a brush, and drained the excess water. To
562 this tube, we added the boiled-to-turbidity heat-fix solution (28% 500 µl NaCl + 5% 200 µl TritonX100 + 19.3
563 ml water), incubated it for ~20 sec with thorough mixing, and then immediately added water to cool down
564 the mixture. Then, we transferred the fixed embryos to 2 ml microfuge tubes, sequentially added n-Heptane
565 and methanol in equal proportions, vigorously shook the tube for about half a minute to break-open and
566 remove the vitelline membrane. This was followed by 3x washes of methanol. Here, we started the staining
567 immediately after, although the embryos can be stored in methanol for long time. The embryos were
568 rehydrated with PBT (0.01% solution of Tween20 in PBS) over 3 washes. Following this we stained the
569 embryos with 1:1000 DRAQ5 for 1 hour. Afterwards, we washed the embryos 6x with PBT, re-suspended
570 them in 3:1 glycerol:PBS solution, and mounted them between 2 rectangular coverslips. The spacing between
571 the coverslips was optimized to keep the embryos in place w/o deforming them. Then we imaged the
572 embryos through both coverslips, and stitched the two half embryos during image analysis to get the full
573 view (see below). Images were acquired on Leica SP8 DMi8 inverted confocal microscope using 20x glycerol
574 objective (0.75NA), with 1.15x digital zoom, at 1 µm step-size in z, and a final x-y resolution of 0.247 µm/pixel.

575 To **visualize the nuclei and F-actin**, we used formaldehyde fixation, and stained the embryos with DAPI and
576 Phallacidin. Briefly, we transferred the processed embryos to 20 ml vial with a brush, which contained the
577 fixation mix (3500 µl PBS + 37% 1000 µl formaldehyde + 4500 µl n-Heptane). The vial was shaken on a
578 platform shaker for 25 minutes @200 rpm. Then, we transferred the fixed embryos to 2 ml microfuge tubes,
579 sequentially added n-Heptane and 90% ethanol in equal proportions, vigorously shook the tube for about
580 half a minute to break-open and remove the vitelline membrane. This was followed by 3x washes of 90%
581 ethanol. Here, we started the staining immediately after, although the embryos can be stored in 90% ethanol
582 for a week or so. The embryos were rehydrated with PBT (0.01% solution of Tween20 in PBS) over 3 washes,

583 following this we stained the embryos with 1:1000 DAPI for 1 hour, followed by 1:500 Phallacidin for 1 hour.
584 Afterwards, we washed the embryos 4x with PBT, re-suspended them in 3:1 glycerol:PBS solution, and
585 mounted them between 2 rectangular coverslips, followed by imaging. Images were acquired on Leica SP8
586 DMi8 inverted confocal microscope using 20x glycerol objective (0.75NA), with 1.2x digital zoom, at 1 µm
587 step-size in z, and a final x-y resolution of 0.473 µm/pixel.

588 Imaging live embryos: We used 4 experimental temperature regimes for embryo live imaging. We collected
589 embryos for 1 hour either at normal temperatures (22-23°C, 24-25°C, or 27-28°C) or elevated temperature
590 (29-30°C). The 22-23°C collections (corresponding to 22°C imaging) were done in the fly incubator. The 24-
591 25°C collections (corresponding to 25°C imaging) were done on the bench top. The 27-28°C collections
592 (corresponding to 28°C imaging) or the 29-30°C collections (corresponding to 29°C imaging) were done in a
593 water bath, where the bottom surface of the embryo collection agar plate is in thermal contact with the
594 heated water. Afterwards, the embryos are washed with bleach for 35-40 seconds, then washed thoroughly
595 with tap water at the same temperature as embryo collection. We then aligned the embryos on a 25 mm
596 diameter circular coverslip, covered them with halocarbon oil, and immediately transferred them to the
597 temperature controller setup on the microscope that's pre-equilibrated to the experimental temperatures
598 for normal temperature regime, (22, 25, or 28°C) or the elevated temperature regime (29°C). We used the
599 temperature controller setup from Warner instruments (locally supplied by MultiChannelSystems). The setup
600 consists of; QR-40LP, which holds the 25mm coverslip with embryos; QE-1HC, which heats/cools QR-40LP
601 along with the embryos mounted in it; LCS-1, the liquid cooling system that isolates the QE-1HC from the
602 effect of ambient temperature; and CL-100, the bipolar temperature controller that can impart the
603 temperature of interest against the baseline set by LCS-1. We mounted QE-1HC on the microscope stage,
604 with LCS-1 and CL-100 as the peripherals controlling the temperature. Images were acquired on Leica SP5
605 DMI6000CS inverted confocal microscope using 40x water objective (1.1NA), with 1x digital zoom, at 2 µm
606 step-size in z with 20 z-steps overall, and a final x-y resolution of 0.379 µm/pixel. As mentioned in the main
607 text, we acquired images starting from interphase 10 or before, till the beginning of gastrulation movements.
608 We recorded the timelaspe at a frame rate of 1 frame every 30 sec, 1 min, or 2 min depending on whether
609 we recorded at a time 1, 2, or 3-4 embryos in parallel.

610 Image analysis and statistics: All image analysis was done using FIJI freeware. There are 7 different kinds of
611 image analyses presented in the manuscript. These are; one, whole embryo reconstruction to see distribution
612 of nuclei in the entire embryo (fixed embryos); two, the analysis of mitotic failures (live embryos); three, the
613 analysis of nuclear movements (live embryos); four, analysis of nuclear cycle asynchrony (live embryos); five,
614 analysis of nuclear crowding (live embryos); six, analysis of the fraction of mitotic failures (live embryos); and
615 seven, comparing the distribution of nuclei alongside that of F-actin (fixed embryos). All the statistical analysis
616 was done using Prism (GraphPad). This includes, the curve fitting (see below, the analysis of nuclear
617 crowding), estimating the non-parametric statistical significances, and estimating the 95% confidence
618 intervals (CI) on the medians. The straight-line fits for analysis of nuclear movements were done using ImageJ
619 macro language.

620 In the **analysis to reconstruct the nuclear distribution in the whole embryo**, we used a custom-built image
621 analysis pipeline to fuse the halves of the same embryo, followed by the computing the distance of each
622 point inside the embryo from the embryo surface. Here we refer to the two views of the embryo as "half
623 embryo", even though in reality the volume in either "half" spans about 70-75% of the embryo width,
624 providing a significant overlap between the two halves. In the pipeline, we process the raw images, stitch the
625 two half embryos, render the fused embryo in lateral view, segment the embryo volume, and then segregate
626 the nuclei as a function of their distance from the surface of segmented embryo volume. First, we processed
627 the raw images: to improve visualization of the nuclei, we used 'Minimum 3D' filter with radii x=y=1, and z=3,

628 and to reduce noise, we used 'Median 3D' filter with radii x=y=z=1. Then, we homogenized the
629 brightness/contrast between the two half embryos. Following these steps, we manually aligned the half
630 embryos along their AP axis, and then used the BigWarp (Bogovic et al. 2016) package in the BigDataViewer
631 ecosystem (Pietzsch et al. 2015) to align the half embryos using manually selected interest points. Essentially,
632 we selected either subcortical- or yolk-nuclei that could be identified in both half embryos. We further
633 cropped the output images to keep only a small margin around the embryo with "aligned halves", in order
634 to reduce the computational load in the steps to follow. After the manual alignment step, we used BigStitcher
635 (Preibisch, Saalfeld, and Tomancak 2009) to further align embryo, using phase correlation method, to
636 produce the "fused embryo". In case of many embryos, additional manual transforms were necessary to
637 produce a fused embryo that passes visual inspection. The fused embryos were then rotated as necessary,
638 and resliced to produce lateral views. Following this, we processed the fused embryo to separate the regions
639 of embryo that contain cortical-, subcortical, and yolk-nuclei. First, we used the nuclear signal to segment the
640 embryo volume, using simple thresholding. This generated a binary image that corresponds to the embryo
641 volume. Then using '3D Distance Map' (plugin in the 3DSuite), we compute the Euclidian distances in 3D, i.e.,
642 each pixel inside the embryo gets the grayscale value corresponding to its distance from the embryo surface.
643 All pixels with Euclidian distance <10 µm would be considered as the cortical layer, those within range of 10-
644 30 µm would be consider subcortical, and those farther than 30µm from embryo surface would be considered
645 as part of the yolk region. These distances are determined empirically, using approximate measurements
646 from various fused embryos. Typically, nuclei have the diameter of 5-10 µm depending on the phase of
647 nuclear division cycle, while the cell height at the end of cellularization is about 30 µm. The pixels in these
648 regions were then color coded and presented as either as maximum projections or cross-sectional views in
649 Figure S2.

650 In the **analysis of mitotic failures**, we tracked expelled nuclei back in time to identify the mitosis when they
651 were born, and to categorize the expulsion as pairwise or isolated (see examples respectively in Figure 1F
652 and Figure S3D). We considered a nucleus to be expelled, if its apical-most tip was at least 12 µm away from
653 the embryo surface. To simplify the identification of expelled nuclei, we color-coded the Histone-RFP signal
654 as a function of distance from the embryo surface. This is similar to above analyses, except we use the
655 'LocalZPojector' plugin in FIJI (Herbert et al. 2021) to define the distance from the embryo surface, while to
656 predict the embryo surface itself we use the Jupiter-GFP signal, which was co-imaged with Histone-RFP. Thus,
657 first we color-code the nuclei, and then manually identify and count the number of pairwise or isolated
658 nuclear expulsions during interphase 14.

659 In the **analysis of nuclear movements**, for a select few nuclei we manually tracked the entire progeny,
660 starting from the mother nucleus in late interphase 10 till the 8 great-granddaughter nuclei at late interphase
661 13. Assigned all of these nuclei to a single cluster, we then calculated the center of the cluster at each time
662 point. We chose nuclei along one continuous row at interphase 10, and tracked their progeny in their
663 individual clusters. For sake of simplicity and consistency, we only chose those nuclear clusters whose entire
664 progeny could be tracked, i.e., we could follow the cluster and see the formation of all 8 great-granddaughter
665 nuclei in interphase 13. This way, we obtained ≥ 13 clusters in any embryo that we tracked. For each of these
666 nuclear cluster trajectories, we fitted a straight-line to coordinates for the center of the cluster, over time
667 (dashed lines in Figure S5B). Then, we calculated the distance of the center of the nuclear cluster to this line
668 at every timepoint. An average of these distances over a specific time period was used as an estimate for
669 deviations in the center of nuclear clusters over that time period. We observed that the clusters move
670 significantly starting from anaphase till a few minutes into the subsequent interphase, as the clusters return
671 to their normal position. Thus, we decided to separately analyze these periods of extensive movement vs.
672 the periods when the cluster movement was low. To identify the periods of extensive movements

consistently and objectively, we noted that these movements start at least 1 timepoint (30 sec) before we could see the first telophase in any of the tracked clusters, while the movements mostly subside within 3 minutes after all of the nuclear clusters finished telophase. Thus, we defined the window of extensive movement as starting from 30 sec before appearance of first telophase nuclei, till 3 min after the appearance of last telophase nuclei. Once we had an objective definition of various time periods, it was straightforward to calculate the average deviation in the center of nuclear clusters.

In the **analysis of asynchrony in nuclear cycles**, we marked various timepoints in the timelapse recordings to follow the progression of nuclear cycles in the anterior-, middle-, and posterior-5th of the field of view. For sake of simplicity, we marked the transitions from a telophase 13 to interphase 14, i.e., the first timepoint when the daughter nuclei in any region go from telophase 13 to interphase 14. If the timepoint for this occurance in the anterior is 'T_a', that in posterior is 'T_p', while the same in the middle is 'T_m', then the 'asynchrony' can be calculated as,

$$asynchrony = T_m - \left(\frac{T_a + T_p}{2}\right)$$

Essentially, we started with the expectation that T_m should be the average of T_a and T_p (maximum synchrony), and a deviation from this expected value would be the asynchrony. Figure S7 diagramatically demonstrates this analysis.

In the **analysis of nuclear crowding**, we analyzed the distribution of nuclei at the end of interphases, as that's the time when the distribution is as stable as it can be, with maximum crowding, if any. To assess nuclear crowding, we started with segmentation of nuclei in the field of view. Here, we used the 'Find Maxima' command to identify local intensity maxima, and imprinted those on an image. Many of these maxima marked a nucleus. We did manual corrections to, remove the maxima that didn't correspond to a nucleus, add a maximum for nuclei that didn't have a maximum associated with them, or correct the maxima that were too off-center from the corresponding nucleus. Then we used Voronoi tessellation to mark territories around these maxima to generate pseudo-cells. We excluded territories that, touched the edge of the image, that had aberrant shapes (aspect ratio>2), or those with aberrant pixel intensities (pseudo cell containing pixels with <5 units of intensity, typically the case with ill-defined pseudo-cells at the edge of segmentation). Thus, each nucleus was associated with a pseudo-cell area value ('Area' in μm^2), and an x-coordinate value for the center of the pseudo-cell ('X' in µm) (x-axis of the image aligned with anterior-posterior axis of the embryo). We fitted these with the equation of a parabola such that 'Area' can be expressed as a function of 'X',

$$Area = aX^2 + bX + c$$

Here, the curvature of the parabola will be higher in case of greater nuclear crowding (compare Figure 2L-O). Thus, the fit parameter 'a', which dictates the curvature of the parabola, was used to estimate the extent of crowding.

In the **analysis of the fraction of mitotic failures**, we tracked expelled nuclei back in time same as the analysis for mitotic failures, except now we also recorded where the nuclei were lost from, to get a map of the locations of mitotic failure in the field-of-view. In parallel, we generated regions in the embryo that correspond to maximum nuclear crowding, maximum delay in nuclear divisions, and a combination of the two regions. To construct the *crowded regions* (the region corresponding to maximum nuclear crowding) we referred to previous studies, which have argued that a certain threshold of nuclear content will halt the syncytial nuclear division cycles (Edgar, Kiehle, and Schubiger 1986), while this threshold was determined to be ~70% of the normal cellularization nuclear density (Lu et al. 2009). Here, we argue that such threshold

715 nuclear content is reached in regions with nuclear crowding, albeit only locally, and should locally trigger an
716 arrest of nuclear divisions, in conflict with rest of the embryo. Another previous study reported the nuclear
717 domain area (i.e., the pseudo-cell area) to be 28.8 μm^2 at cellularization (Telley et al. 2012). We corroborate
718 this number with our own quantifications (data not shown). For simplicity of calculations, we assume that
719 *Drosophila* embryos have 6000 nuclei at interphase 14 each with an area of 29 μm^2. The 70% density of nuclei
720 would thus correspond to 4200 nuclei at interphase 14, each with an area of 41.43 μm^2, which we
721 approximate to 42 μm^2. Thus, the back of the envelop calculation indicated that nuclei will seize to divide
722 when their pseudo-cell area drops below ~42 μm^2. We observed that in embryos developing at 29°C, the
723 central regions of the embryo contained many nuclei that had pseudo-cell areas less than 42 μm^2, already at
724 interphase 13. Thus, we used this criterion to define areas of embryos that have likely reached the 70%
725 cellularization nuclear density, at one nuclear division cycle earlier, albeit only locally. Since the embryos at
726 normal temperatures (22, 25, and 28°C) rarely have nuclei with pseudo-cell areas smaller than 42 μm^2, we
727 further decided to include all nuclei with pseudo-cell areas in the lower quartile to construct the region with
728 maximum nuclear crowding. Here we also note that this description is only a rationalization of the approach,
729 and that it is not a comment on how the effect of nuclear crowding might actually manifest. For instance, it
730 is also likely that mitotic spindles are not properly established in the crowded regions, thus causing the
731 mitotic failure. However, this wouldn't allow us to define equivalent regions in the embryos at normal
732 temperatures, as it is not feasible to accurately define the size of the mitotic spindle, in our experiments.
733 Then, to construct the *delayed region* (the region with maximum delay in nuclear divisions), we simply
734 marked the areas of the embryo that contain the last ~20% of the nuclei that finished nuclear cycle 13. This
735 percentage was decided empirically: it corresponds to a region of similar size as that corresponding to the
736 crowded regions above. Here the rationale is drawn from previous studies which indicate that the regulation
737 of nuclear division cycles is coordinated at the scale of the entire embryo (Deneke et al. 2016), and given that
738 all of the nuclei share the same cytoplasm, a local delay in nuclear cycles would create conflicts between the
739 biochemical status of the cytoplasm and the cell cycle stage of the delayed nuclei. Finally, to construct the
740 *combined region* (combination of crowded and delayed region), we used the logical OR operator to combine
741 the crowded and delayed regions, to test combinatorial effects of the nuclear crowding and nuclear cycle
742 asynchrony. In the end, we computed the fraction of mitotic failures in the crowded, delayed, or combined
743 regions using,

744 $$fraction\ of\ mitotic\ failures = \frac{number\ of\ mitotic\ failures\ in\ a\ specific\ region}{total\ number\ of\ mitotic\ failures}$$

745 In the **analysis to compare the distribution of nuclei alongside that of F-actin**, was rather similar to the
746 pipeline to *reconstruct the nuclear distribution in the whole embryo*, except that we didn't have 2 half-
747 embryos to fuse, essentially starting from segmentation of embryo volume. Here, instead of using nuclear
748 staining, we segmented embryo volume using the F-actin staining. Then the 3D distance map similarly
749 allowed us to classify pixels into cortical-, subcortical-, or yolk-regions based on their distance from embryo
750 surface. The pixels in these regions were then color coded and presented as sum projections in Figure S9.

751 **Figure and table legends:**

752 **Figure 1: Embryonic lethality and the loss of nuclei due to mitotic failures in embryos exposed to elevated**
753 **temperature.**
754 (A, B) To assess developmental robustness, we exposed embryos to various temperature regimen and
755 estimated the embryo lethality. (A) Schematic showing the temperature regimen in the embryo survival
756 experiment, starting from the beginning of embryo collection. Here we have three conditions depending on
757 exposure to normal or elevated temperature regimen in the 3-hour time windows as shown, normal-normal

758 [NN], elevated-normal [EN], and normal-elevated [NE]. In all cases, the first time-window also includes 1 hour
759 of embryo collection. The embryonic development beyond 6 hours continued at normal temperature. (B) The
760 scatter plots show the distribution of percent lethality in embryos from various conditions, calculated based
761 on the fraction of embryos that don't hatch into larvae. Each dot represents data from a sample with ≥26
762 embryos; n= 12 (NN), 10 (EN), 10 (NE) samples.

763 (C-E) Montages of snapshots from live embryos, expressing Histone-RFP, from late interphase 11 till late
764 interphase 14, in embryos developing either at normal temperatures (C), or at elevated temperature showing
765 mild (D), or severe (E) defect. The nuclei were labelled as a function of their distance from the embryo surface.
766 Here, green indicates cortical, and magenta indicates sub-cortical nuclei that are lost. At elevated
767 temperature, a lot more nuclei are expelled, and as a result, we can see large gaps between cortical (green)
768 nuclei, often coinciding with expelled (magenta) nuclei, especially during early interphase-14.

769 (F-H) To assess the pairwise loss of nuclei, we counted mitotic failures that lead to such nuclear expulsions.
770 (F) Montage of snapshots from live embryo, from late interphase 12 to late interphase 13, where Histone-
771 RFP marks the distribution of nuclei, cortical nuclei are in green and subcortical (expelled) nuclei are in
772 magenta. The pairwise loss of nuclei due to mitotic failure is exemplified in an embryo developing at elevated
773 temperature. The arrowheads track the segregating daughter nuclei that will be expelled eventually, while
774 arrows exemplify normal nuclei. Of note, this type of nuclear loss occurs at all temperatures, though at
775 different a frequency. (G) Scatter plot showing the distribution of events of nuclear losses due to mitotic
776 failure during interphase 14. n= 10 (22°C), 7 (25°C), 9 (28°C), and 10 (29°C) embryos. (H) The schematic to
777 illustrate the phenomenon of mitotic failures at elevated temperature.

778 Scale bars; C-E, 25 µm; F, 5 µm. B and G show scatters with median, with whiskers showing 95% CI. In G, the
779 hollow markers indicate embryos that have a blastoderm hole, with large hollow markers indicating a single
780 large hole, and small hollow markers indicating either a single or multiple small holes. *, $p<0.05$; **, $p<0.01$;
781 ***, $p<0.001$; ****, $p<0.0001$, non-significant comparisons are not shown.

782 **Figure 2: Nuclear cycle asynchrony and nuclear crowding increases as a function of temperature during**
783 **embryo development.**
784 (A-C) To assess the asynchrony in nuclear cycles, we identified the phases of nuclear cycle along the AP axis.
785 (A) Image shows the entire anterior-posterior extent of the field of view, from a live embryo developing at
786 29°C. Histone-RFP marks the nuclei, cortical nuclei are in green and subcortical (expelled) nuclei are in
787 magenta. Different regions of the embryo have nuclei in different stages of nuclear division cycle, as indicated
788 above the image. Arrows show the direction in which the wave of nuclear division cycle will progress. Here,
789 we have an anterior- and a posterior-wave which will meet in the central region of the embryo. The anterior,
790 central, and posterior 1/5th of the field of view are indicated below the image, with the anterior 1/5th of the
791 embryo containing nuclei that are more advanced in division cycle, as compared to the posterior 1/5th, which
792 are yet more advanced than the central 1/5th. As a result, these regions will enter the subsequent interphase
793 in an asynchronous manner (see also Figure S7). (B) Scatter plots showing the distribution of asynchrony for
794 embryos at various temperatures. n= 10 (22°C), 7 (25°C), 9 (28°C), and 10 (29°C) embryos. (C) The schematic
795 illustrates the progressive increase in asynchrony at elevated temperature.

796 (D-Q) To assess the crowding of nuclei, we segmented the nuclei and generated pseudo-cells. The figure
797 shows data from of live embryos that were developing either at 22°C (D, H, L), 25°C (E, I, M), 28°C (F, J, N), or
798 at 29°C (G, K, O). (D-G) Snapshots from live embryos at the end of interphase 13, where Histone-RFP marks
799 the nuclei. The outline shows the region of the image that is considered for quantifications. (H-K) The pseudo-
800 cells for the corresponding embryos in D-G. A pseudo cell is centred on a nucleus, while the region of a
801 pseudo-cell is bound by line segments that are equidistant from neighbouring nuclei. Various pseudo-cells

are colour-coded according to their area in μm^2 according to the LUT at the bottom. (L-O) Plots showing the distribution of pseudo-cell areas as a function of their anterior-posterior position, along with a quadratic fit through the distribution, for embryos in D-G. (P) Scatter plots showing distribution of the coefficient of the quadratic term for embryos at various temperatures. This essentially captures the extent of nuclear crowding, with larger quadratic coefficient indicating greater crowding. n= 10 (22°C), 7 (25°C), 9 (28°C), and 10 (29°C) embryos. (Q) The schematic illustrates the crowding effect at elevated temperature. The size of the black arrows indicates the gradation in nuclear density, from poles to the central region.

Scale bars, 20 µm. B and P shows scatters with median, with whiskers showing 95% CI. In B and P, hollow markers indicate data from embryos that have blastoderm hole, with large hollow markers indicating a single large hole, and small hollow markers indicating either a single or multiple small holes. *, $p<0.05$; **, $p<0.01$; ***, $p<0.001$; non-significant comparisons are not shown.

Figure 3: Nuclear crowding and nuclear cycle asynchrony combinatorially enhance mitotic failure defect.
(A, B) Snapshots from live embryo, developing at 29°C, at the end of interphase 13 (A), and 14 min afterwards (B), where Histone-RFP marks the nuclei. The outline in A shows the region of the image that is has nuclear crowding, while that in B bounds the region containing most delayed nuclei, i.e., those that are most lagging in nuclear division cycles.

(C-E) The locations of lost pairs of nuclei during interphase 14 are marked as white dots to indicate their distribution in the field of view. Then, various regions are defined in the embryo to illustrate the fraction of mitotic failures occurring in that region. These regions are composed based on, the crowded region (C), the delayed region (D), and the combined region (E).

(F-K) Scatter plots showing the distribution of the area fractions in crowded (F), delayed (G), and combined (H) regions of the embryos. In case of both crowded (F) and delayed (G) regions, the medians are rather comparable across temperature, and the low variability within a given temperature is exaggerating the differences across temperatures. In case of the area fraction of the combined regions (H), the increase in the overlap of crowded and delayed region reduces the overall size of the combined regions. Then, scatter plots showing the distribution of fraction of mitotic failures occurring in the crowded region (I), in the delayed region (J), and in the combined regions (K). n= 10 (22°C), 7 (25°C), 9 (28°C), and 10 (29°C) embryos.

Scale bars, 20 µm. F-K show scatters with median, with whiskers showing 95% CI. Hollow markers indicate data from embryos that have blastoderm hole, with large hollow markers indicating a single large hole, and small hollow markers indicating either a single or multiple small holes. *, $p<0.05$; **, $p<0.01$; ***, $p<0.001$; non-significant comparisons are not shown.

Figure 4: Rescue of embryonic lethality at elevated temperature through over-expression of the regulators of cell polarity signalling or those of F-actin -microtubules interaction during mitosis, and genes varying along thermoclines as "natural" candidates.
(A-C) Testing the rescue of embryonic lethality and fraction of mitotic failures with over-expression of *baz* and *dlg*. (A) Scatter plot showing the distribution of percent lethality in embryos from various genotypes, at normal (25°C) vs elevated temperature (29°C), calculated based on the fraction of embryos that don't hatch into larvae. Each dot represents data from a sample with ≥12 embryos; control, n= 9 (22°C), 9 (29°C) samples; baz-OE, n= 11 (22°C), 10 (29°C) samples; dlg-OE, n= 12 (22°C), 10 (29°C) samples. Scatter plots showing the distribution of the fraction of mitotic failures in crowded regions (B), and in crowded OR delayed regions (C), in the embryos at normal (22°C) vs elevated temperature (29°C). Each dot represents data from one embryo: control, n= 7 (22°C), 9 (29°C) embryos; baz-OE, n= 7 (22°C), 7 (29°C) embryos; dlg-OE, n= 6 (22°C), 7 (29°C) embryos. Additional quantifications related to this experiment are presented in Figure S8.

845 (D-F) Testing the rescue of embryonic lethality and fraction of mitotic failures with over-expression of *αCat*
846 and *sgg*. (D) Scatter plots showing the distribution of percent lethality in embryos from various genotypes,
847 at normal (25°C) vs elevated temperature (29°C), calculated based on the fraction of embryos that don't
848 hatch into larvae. Each dot represents data from a sample with ≥18 embryos; control, n= 10 (22°C), 11 (29°C)
849 samples; αCat-OE, n= 10 (22°C), 12 (29°C) samples; sgg-OE, n= 8 (22°C), 7 (29°C) samples. (E, F) Scatter plots
850 showing the distribution of the fraction of mitotic failures in crowded regions (E), and in crowded OR delayed
851 regions (F), in the embryos at normal (22°C) vs elevated temperature (29°C). Each dot represents data from
852 one embryo: control, n= 8 (22°C), 9 (29°C) embryos; αCat-OE, n= 8 (22°C), 8 (29°C) embryos; sgg-OE, n= 7
853 (22°C), 7 (29°C) embryos. Additional quantifications related to this experiment are presented in Figure S10.

854 (G) Pie charts showing the clinal distribution score for various genes associated with 'spindle dynamics'
855 (combination of GO terms, cell polarity, spindle organisation, and spindle localisation, n=320 genes), or with
856 GO term 'metabolic process' (n=6612 genes). ~40% of genes associated with spindle dynamics, while ~30%
857 of the genes associated with metabolic process, are clinal in at least one continent.

858 A-F shows scatters with median, with whiskers showing 95% CI. In B, C, E, and F, hollow markers indicate data
859 from embryos that have blastoderm hole, with large hollow markers indicating a single large hole, and small
860 hollow markers indicating either a single or multiple small holes. *, $p<0.05$; **, $p<0.01$; ***, $p<0.001$; ****,
861 $p<0.0001$; non-significant comparisons are not shown.

862 **Figure S1: Blastoderm holes appear in a fraction of embryos at elevated temperature.**
863 The figure shows the snapshots from live embryos, expressing Histone-RFP, from early interphase 14, in
864 embryos developed at elevated temperature. The nuclei are labelled as a function of their distance from the
865 embryo surface. Here, green indicates cortical, and magenta indicates sub-cortical nuclei that are expelled,
866 while arrows/arrowheads indicate large/small blastoderm holes. For embryos with large blastoderm holes
867 (embryo 05, and 08), we see many nuclei in magenta, while in case of embryos with small blastoderm holes
868 (embryos 04, and 09), we can see only a few nuclei in magenta per hole. We would argue that development
869 in *Drosophila* is robust enough to buffer the defects due to the small holes, but fails at 29°C when large holes
870 appear.

871 Scale bar, 25 µm.

872 **Figure S2: Nuclear loss shows left-right asymmetry in embryos developing at elevated temperature.**
873 Distribution of nuclei in embryos during interphase 13, in fixed embryos that were developing either at
874 normal temperature (A, D, G, H), or at elevated temperature that show either a mild defect (B, E, I, J) or a
875 severe defect (C, F, K, L). (A-F) Maximum projections of the right and left halves of embryos, where the nuclei
876 are labelled as a function of their distance from the embryo surface. Here, green indicates cortical nuclei, i.e.,
877 nuclei close to embryo surface, while magenta indicates sub-cortical nuclei, i.e., nuclei that are deeper in the
878 embryo, farther from embryo surface. The yolk nuclei are not shown for improved visibility. As compared to
879 embryos at normal temperature (A), those at elevated temperature show mildly (B) or severely (C) numerous
880 gaps in the distribution of cortical nuclei. These gaps often also correspond to the locations of subcortical
881 nuclei (A-C). Of note, the embryo surface prediction gets distorted at the posterior pole, due to the pole cell
882 nuclei that are outside the embryo cortex, thus mislabelling cortical nuclei in magenta. These mis-coloured
883 nuclei were manually erased to exclusively highlight the subcortical nuclei (D-F). (G-L) Cross-sectional view
884 along the indicated regions in panels A-C. Here, yolk nuclei are additionally marked in yellow. The arrow
885 indicates the direction along which we can follow the surface of the embryo along the cross-section. The
886 cross-sections are chosen to specifically highlight the locations of subcortical nuclei.

887 Scale bars; A-C, 50 µm; G, I, and K, 25 µm.

Figure S3: Out-of-plane nuclear divisions during mitosis 10, and the low frequency of isolated nuclear expulsion during interphase 14, does not vary significantly with temperature, and cannot explain the observed loss of nuclei.

(A, B) Montages exemplifying out-of-plane division during mitosis 10 in an embryo developing at 25°C. Histone-RFP marks the nuclei (green), while Jupiter-GFP marks the microtubules (magenta). Arrowheads exemplify in-plane divisions, while arrows exemplify out-of-plane division. Each subsequent frame is 1 min apart. In the x-y view of the divisions (A), only one of the daughter nuclei is clearly visible after the out-of-plane division, while the other daughter nucleus is better seen in the y-z view of the division (B), where we can see it translocating to the embryo interior. (C) Plots show the number of out-of-plane divisions, that are visible in the field of view, in embryos developing at various temperatures. For context, an embryo contains on the order of 70 mitotic spindles the field of view at interphase 10. So, even though the p-value is <0.05 for the comparison between 22°C and 29°C, we would argue that the difference is not biologically significant, given that there is no correlation between the number of out-of-plane divisions and the presence of blastoderm holes. n= 10 (22°C), 7 (25°C), 9 (28°C), and 10 (29°C) embryos.

(D) Montage exemplifying isolated nuclear expulsion in an embryo developing at 25°C, from telophase 12 to late interphase 13. Histone-RFP marks the distribution of nuclei, cortical nuclei are in green and subcortical (expelled) nuclei are in magenta. The arrowheads track the daughter nucleus that will be expelled, while arrows track the daughter nucleus that will be retained cortically. (E) Scatter plots showing the distribution of isolated loss of nuclei during interphase 14. n= 10 (22°C), 7 (25°C), 9 (28°C), and 10 (29°C) embryos.

Scale bar; A, 10 µm; D, 5 µm. C and E show scatters with median, with whiskers showing 95% CI. The hollow markers indicate embryos that have a blastoderm hole, with large hollow markers indicating a single large hole, and small hollow markers indicating either a single or multiple small holes. *, p<0.05; non-significant comparisons are not shown.

Figure S4: Defective nuclei take different amount of time to be expelled from embryo cortex.

(A, B) The figure shows the montages of snapshots from live embryos, with a few representative nuclei tracked from late interphase 12 to interphase 13. Top panels show Histone-RFP signal, while bottom panels show Jupiter-GFP signal. Nuclei tagged in green/magenta are the ones that arise from mitotic defects during mitosis 10/11. All of these are expelled during interphase 13. Notice the lack of spindle formation around the tagged nuclei. Also note that the nuclei expelled by the 5th timepoint are not shown in the 6th timepoint. (A) An embryo developing at normal temperature, where 1 magenta and 1 green nuclei are followed. (B) An embryo developing at elevated temperature, where 6 magenta and 3 green nuclei are followed.

Scale bars, 20 µm. The numbers in inset indicate time in min:sec.

Figure S5: Nuclear movement parallel to the embryo surface is amplified at elevated temperature.

(A-C) An example depicting how the nuclear movements are tracked, and the deviations thereof are calculated. Snapshots from live embryo developing at elevated temperature, where Histone-RFP marks the distribution of nuclei, showing the mother nuclei at the end of interphase 10 (A) and the corresponding 8 great-granddaughter nuclei, each, at the end of interphase 13 (C). The neighbouring nuclear clusters are marked in either cyan or yellow. The trajectories of the center of nuclear clusters (B) also indicate the increase in the number of nuclei due to divisions, as the broadening of the tracks. The dotted lines indicate straight-lines fitted to individual trajectories, which are used as reference for computing deviations for each time point of that trajectory. The shaded region captures periods of greatest movement that starts with anaphase (see methods).

930 (D-I) To quantify the drift in the center of nuclear clusters, we compute the slope of the straight-line fits
931 (dotted lines in B). The median of slopes for all nuclear cluster from one embryo provides a robust estimate
932 of the drift in the centers of the nuclear clusters. Plots showing the distribution of these medians (one dot
933 per embryo), for the drift along AP axis (D), and for that along DV axis (E). To quantify the movements in the
934 center of nuclear clusters during periods of maximum movement (shaded region in B) and normal movement
935 (unshaded regions in B), we compute the average of the deviations from the straight-line fits (dotted lines in
936 B). The median of such average deviations for all nuclear cluster from one embryo provides a robust estimate
937 of the nuclear cluster deviation. Plots showing the distribution of these medians (one dot per embryo), for
938 the fluctuations along AP axis (F, H), and for those along DV axis (G, I), during interphase-metaphase (F, G) or
939 during anaphase-telophase (H, I). n= 10 (22°C), 7 (25°C), 9 (28°C), and 10 (29°C) embryos.

940 Scale bar, 25 µm. D to I show scatters with median, with whiskers showing 95% CI. Hollow markers indicate
941 data from embryos that have blastoderm hole, with large hollow markers indicating a single large hole, and
942 small hollow markers indicating either a single or multiple small holes. *, $p<0.05$; **, $p<0.01$; ***, $p<0.001$;
943 non-significant comparisons are not shown.

944 **Figure S6: Nuclear movement along surface-yolk axis is amplified at elevated temperature.**
945 Cross-sections from live embryos, expressing Histone-RFP, from late interphase 13 till early interphase 14, in
946 embryos developing either at normal temperature (A), or at elevated temperature (B). Here, the coloured
947 lines mark the basal tip of nuclei in the first frames (t=-7:30 min) of the respective montage. Timepoint 00:00
948 corresponds to initiation of anaphase at the left/right extreme of the images, which is also the first time we
949 see the shift from baseline.

950 Arrowheads point out the local peak of the nuclear shift from the baseline, while arrow points expelled nuclei.
951 As we can see, at elevated temperature, the nuclei shift significantly from the baseline, before returning to
952 normal localisation by the time the nuclei enter the subsequent interphase. Also, the shift from baseline
953 occurs progressively from anterior/posterior poles towards the central region.

954 Scale bars, 25 µm. Cross-sections are in the lateral region of the embryos, anterior to the left.

955 **Figure S7: Nuclear cycle asynchrony increases as a function of the temperature during embryo**
956 **development.**
957 (A, B) Montages of snapshots from metaphase 13 to early interphase 14, from live embryos developing either
958 at 25°C (A), or at 29°C (B). Histone-RFP marks the nuclei, cortical nuclei are in green and subcortical (expelled)
959 nuclei are in magenta. The dotted lines divide the field of view in 5 equal parts. Numbers in the inset
960 represent time in min:sec, while 00:00 is when anterior $1/5^{th}$ of the embryo enters interphase 14. Boxes
961 highlight entry into interphase 14 in that region. The black arrows indicate the time point of maximum
962 synchrony, i.e., halfway between the anterior and posterior $1/5^{th}$ of the embryo, when the nuclei in the
963 central region should have entered interphase 14. This point serves as the reference to estimate asynchrony
964 (see methods).

965 Scale bars, 25 µm.

966 **Figure S8: Additional quantifications related to *baz* or *dlg* over-expression.**
967 (A-F) The distribution of the pseudo-cell areas in embryos at the end of interphase 13, in live embryos
968 developing either at normal temperatures (A, C, and E), or at elevated temperature (B, D, and F). The pseudo-
969 cell areas in embryos of control genotype (A, B), in embryos over-expressing *baz* (C, D), or in embryos over-
970 expressing *dlg* (E, F), are shown. Anterior is to the left, dorsal up. The LUT bar at the bottom indicates the
971 colour code corresponding to the area of pseudo-cells.

(G-K) Scatter plots showing the distribution of the area fractions in crowded (G), and combined (H) regions of the embryos, the distribution of the extent of nuclear crowding (I), the distribution of the nuclear cycle asynchrony (J), and the number of pairwise nuclear expulsions (i.e., the number of mitotic failures) (K) for embryos from various genotypes, at normal (22°C) vs elevated temperature (29°C). Each dot represents data from one embryo: control, n= 7 (22°C), 9 (29°C) embryos; baz-OE, n= 7 (22°C), 7 (29°C) embryos; dlg-OE, n= 6 (22°C), 7 (29°C) embryos.

Scale bar, 25 µm. G-K show scatters with median, with whiskers showing 95% CI. Hollow markers indicate data from embryos that have blastoderm hole, with large hollow markers indicating a single large hole, and small hollow markers indicating either a single or multiple small holes. *, p<0.05; **, p<0.01; ***, p<0.001; non-significant differences are omitted.

Figure S9: Elevated temperature disrupts the association between nuclei and F-actin caps.
Distribution of nuclei and F-actin in embryos during interphase 13, in fixed embryos that were developing either at normal temperatures (A, C, D), or at elevated temperature (B, E, F). (A, B) The images show SUM projections of the DAPI stained nuclei (top image) and Phallacidin stained F-actin (bottom image) of representative embryos. In the top images, the nuclei are labelled as a function of their distance from the embryo surface, where green indicates cortical, and magenta indicates sub-cortical nuclei. The yolk nuclei are not shown. Anterior is on the left, dorsal up. (C-F) The top and bottom images show a zoomed-in view of the indicated regions in panels A and B. Here, arrowheads indicate the expelled nuclei (C, E top panels) and the structures of F-actin corresponding to them (C, E bottom panels), which should otherwise be localised around cortical nuclei. Then, the arrows indicate gaps between neighbouring nuclei (D, F top panels), which should normally be devoid of any F-actin structures (D, bottom panel), but contain small "actin caps" in embryos at elevated temperature (F, bottom panel).

Scale bars, 25µm. The boxed regions are 60x60 µm.

Figure S10: Additional quantifications related to *αCat* or *sgg* over-expression.
(A-F) The distribution of the pseudo-cell areas in embryos at the end of interphase 13, in live embryos developing either at normal temperatures (A, C, and E), or at elevated temperature (B, D, and F). The pseudo-cell areas in embryos of control genotype (A, B), in embryos over-expressing *αCat* (C, D), or in embryos over-expressing *sgg* (E, F), are shown. Anterior is to the left, dorsal up. The LUT bar at the bottom indicates the colour code corresponding to the area of pseudo-cells. (G-K) Scatter plots showing the distribution of the area fractions in crowded (G), and combined (H) regions of the embryos, the distribution of the extent of nuclear crowding (I), the distribution of the nuclear cycle asynchrony (J), and the number of pairwise nuclear expulsions (i.e., the number of mitotic failures) (K) for embryos from various genotypes, at normal (22°C) vs elevated temperature (29°C). Each dot represents data from one embryo: control, n= 8 (22°C), 9 (29°C) embryos; αCat-OE, n= 8 (22°C), 8 (29°C) embryos; sgg-OE, n= 7 (22°C), 7 (29°C) embryos.

Scale bar, 25 µm. G-K show scatters with median, with whiskers showing 95% CI. Hollow markers indicate data from embryos that have blastoderm hole, with large hollow markers indicating a single large hole, and small hollow markers indicating either a single or multiple small holes. *, p<0.05; **, p<0.01; ***, p<0.001; non-significant differences are omitted.

Figure S11: *mud* or *insc* over-expression does not ameliorate embryo survival at elevated temperature.
Scatter plot shows the distribution of percent lethality in embryos from various genotypes, at normal (25°C) vs elevated temperature (29°C), calculated based on the fraction of embryos that don't hatch into larvae. Each dot represents data from a sample with ≥21 embryos; control, n= 10 (22°C), 11 (29°C) samples; mud-OE, n= 11 (22°C), 12 (29°C) samples; insc-OE, n= 7 (22°C), 10 (29°C) samples. As we can see in the plot, neither

1015 *mud* nor *insc* over-expression rescues the embryo lethality at elevated temperature, with *mud* over-
1016 expression increasing embryo lethality even at normal temperature (25°C).

1017 The plot shows scatters with median, while whiskers showing 95% CI. *, p<0.05; **, p<0.01; ***, p<0.001;
1018 non-significant differences are omitted.

1019 **Table S1:** This table contains genes that are identified as being clinal in different continents. Columns A to C
1020 contains lists of studies, and under the studies is a list of genes that are identified in these studies as being
1021 clinal. Column A, B, and C respectively list studies that have data from the continents of Australia and/or
1022 Australasia (AUS), North and/or Central America (USA), and Europe and/or North Africa (EU).

1023 We collect all the genes associated with the GO terms 'cell polarity', 'spindle organization', and 'spindle
1024 localization', to compile a non-redundant master list of candidate genes associated with 'spindle dynamics'
1025 in Column F. For each gene in column F, we count the number of times that gene appears in column A to C,
1026 counting a maximum of once per column, to respectively populate columns G to I. For each gene in column
1027 F, column J contains the sum of values in G, H, and I, to indicate the number of continents in which a gene is
1028 clinal. Each gene gets a score from 1 to 3, and we consider the gene to be a relevant candidate if it is found
1029 in at least 2 columns, i.e., with a score of 2 or 3.

1030 We collect all the genes associated with the GO term 'metabolic process', to compile a control list of
1031 candidate genes in Column L. For each gene in column L, we count the number of times that gene appears in
1032 column A to C, counting a maximum of once per column, to respectively populate columns M to O. For each
1033 gene in column L, column P contains the sum of values in M, N, and O, to indicate the number of continents
1034 in which a gene is clinal. Thus, each gene gets a score from 1 to 3.

1035 Following articles were used to source the list of genes in column A (Oakeshott, McKechnie, and Chambers
1036 1984; McColl and McKechnie 1999; Bettencourt et al. 2002; Frydenberg, Hoffmann, and Loeschcke 2003;
1037 Umina et al. 2005; Sawyer et al. 2006; Weeks, Mckechnie, and Hoffmann 2006; Rand et al. 2010; Kolaczkowski
1038 et al. 2011; Paaby et al. 2014), column B (Vigue and Johnson 1973; Oakeshott, McKechnie, and Chambers
1039 1984; Berry and Kreitman 1993; Duvernell and Eanes 2000; P. S. Schmidt, Duvernell, and Eanes 2000; Verrelli
1040 and Eanes 2001; Duvernell, Schmidt, and Eanes 2003; Sezgin et al. 2004; P. S. Schmidt and Paaby 2008; Rand
1041 et al. 2010; Fabian et al. 2012; Paaby et al. 2014; Machado et al. 2016), and column C (Oakeshott, McKechnie,
1042 and Chambers 1984; Costa et al. 1992; Weeks, Mckechnie, and Hoffmann 2006; Kapun et al. 2020).

1043 **Table S2:** Column A lists candidates from Table S1 column F that have a score of 2 or higher, i.e., those that
1044 show selectable variation in natural populations. For these genes, we query FlyBase
1045 (http://flybase.org/batchdownload) for additional details like, gene name (column B), gene symbol (column
1046 C), and the level of expression for these genes during the first 2 hours of embryo development (column D).
1047 The level of expression is based on published transcriptomics data (Graveley et al. 2011), which would
1048 correspond to maternal pool of mRNAs, the most relevant developmental window for this study. The
1049 candidate genes clinal in all 3 continents are highlighted in green.

1050 Columns F-J present a table with counts of genes that are associated with various categories of genes in Table
1051 S1 column F and L, and a further breakdown of how many of these genes are clinal in how many continents.
1052 The breackdown is also plotted as pie-charts in Figure 4G.

1053 **Table S3:** This table lists various figure panels (columns A and B), and the related parental genotypes, i.e., the
1054 genotypes of females (column C) and males (column D) present in the embryo collection cages for the
1055 experiment related to a figure panel.

1056 **Additional information**

Data and Code Availability:

Data and codes developed for data analysis are available upon request from corresponding authors.

Author contributions:

G.K. and S.L. planned the project. G.K. did the experiments with help from P.A. for baz and dlg overexpressions, and JJ.D.-L. for embryo fixation, and nuclei and F-actin staining. G.K. did the image analyses and statistical analyses. G.K. and S.L. wrote the manuscript, and all authors gave comments on the manuscript.

Acknowledgments:

We would like to thank Lázaro Centanin, Nicolas Gompel, and Marianthi Karageorgi for insightful comments on various drafts of the manuscript, and Lemke lab members for discussions throughout the project. We are grateful to Jochen Wittbrodt for his enthusiasm, and for his continuous and generous support. We would also like to thank Ingrid Lohmann for *Drosophila* culture related support, and Thomas Lecuit for sharing fly lines. We sincerely appreciate the efforts taken by FlyBase for maintaining curated database and Bloomington Drosophila Stock Center for providing transgenic fly lines. This work was funded by the DFG (LE 2787/3-1) to S.L., while G.K. was supported through an HFSP Long-term postdoctoral fellowship (LT000597/2019-L).

Competing interests:

The authors declare no competing financial interest.

References:

Berry, A., and M. Kreitman. 1993. "Molecular Analysis of an Allozyme Cline: Alcohol Dehydrogenase in Drosophila Melanogaster on the East Coast of North America." *Genetics* 134 (3): 869–93. https://doi.org/10.1093/genetics/134.3.869.

Bettencourt, Brian R., Inyoung Kim, A. A. Hoffmann, and M. E. Feder. 2002. "Response to Natural and Laboratory Selection at the Drosophila Hsp70 Genes." *Evolution* 56 (9): 1796–1801. https://doi.org/10.1111/j.0014-3820.2002.tb00193.x.

Bogovic, John A., Philipp Hanslovsky, Allan Wong, and Stephan Saalfeld. 2016. "Robust Registration of Calcium Images by Learned Contrast Synthesis." In *2016 IEEE 13th International Symposium on Biomedical Imaging (ISBI)*, 2016-June:1123–26. IEEE. https://doi.org/10.1109/ISBI.2016.7493463.

Cao, Jian, Justin Crest, Barbara Fasulo, and William Sullivan. 2010. "Cortical Actin Dynamics Facilitate Early-Stage Centrosome Separation." *Current Biology : CB* 20 (8): 770–76. https://doi.org/10.1016/j.cub.2010.02.060.

Chong, Jeronica, Christopher Amourda, and Timothy E. Saunders. 2018. "Temporal Development of Drosophila Embryos Is Highly Robust across a Wide Temperature Range." *Interface* 15 (144). https://doi.org/10.1098/rsif.2018.0304.

Costa, Rodolfo, Alexandre A. Peixoto, Guido Barbujani, and Charalambos P. Kyriacou. 1992. "A Latitudinal Cline in a Drosophila Clock Gene." *Proceedings of Royal Society of London*, 43–49.

Crews, Sarah M., W Tyler McCleery, and M. Shane Hutson. 2016. "Pathway to a Phenocopy: Heat Stress Effects in Early Embryogenesis." *Developmental Dynamics : An Official Publication of the American Association of Anatomists* 245 (3): 402–13. https://doi.org/10.1002/dvdy.24360.

Deneke, Victoria E., Anna Melbinger, Massimo Vergassola, and Stefano Di Talia. 2016. "Waves of Cdk1 Activity in S Phase Synchronize the Cell Cycle in Drosophila Embryos." *Developmental Cell* 38 (4): 399–412. https://doi.org/10.1016/j.devcel.2016.07.023.

Duvernell, David D., and W. F. Eanes. 2000. "Contrasting Molecular Population Genetics of Four Hexokinases in Drosophila Melanogaster, D. Simulans and D. Yakuba." *Genetics* 156 (3): 1191–1201. https://doi.org/10.1093/genetics/156.3.1191.

Duvernell, David D., Paul S. Schmidt, and Walter F. Eanes. 2003. "Clines and Adaptive Evolution in the Methuselah Gene Region in Drosophila Melanogaster." *Molecular Ecology* 12 (5): 1277–85. https://doi.org/10.1046/j.1365-294X.2003.01841.x.

1105 Edgar, Bruce A., Caroline P. Kiehle, and Gerold Schubiger. 1986. "Cell Cycle Control by the Nucleo-
1106 Cytoplasmic Ratio in Early Drosophila Development." *Cell* 44 (2): 365–72.
1107 https://doi.org/10.1016/0092-8674(86)90771-3.
1108 Edwards, Marshall J. 2006. "Review: Hyperthermia and Fever during Pregnancy." *Birth Defects Research.*
1109 *Part A, Clinical and Molecular Teratology* 76 (7): 507–16. https://doi.org/10.1002/bdra.20277.
1110 Fabian, Daniel K., Martin Kapun, Viola Nolte, Robert Kofler, Paul S. Schmidt, Christian Schlötterer, and
1111 Thomas Flatt. 2012. "Genome-Wide Patterns of Latitudinal Differentiation among Populations of
1112 Drosophila Melanogaster from North America." *Molecular Ecology* 21 (19): 4748–69.
1113 https://doi.org/10.1111/j.1365-294X.2012.05731.x.
1114 Figard, Lauren, Liuliu Zheng, Natalie Biel, Zenghui Xue, Hasan Seede, Seth Coleman, Ido Golding, and Anna
1115 Marie Sokac. 2019. "Cofilin-Mediated Actin Stress Response Is Maladaptive in Heat-Stressed
1116 Embryos." *Cell Reports* 26 (13): 3493-3501.e4. https://doi.org/10.1016/j.celrep.2019.02.092.
1117 Foe, V. E., and B. M. Alberts. 1983. "Studies of Nuclear and Cytoplasmic Behaviour during the Five Mitotic
1118 Cycles That Precede Gastrulation in Drosophila Embryogenesis." *Journal of Cell Science* 61 (May): 31–
1119 70. https://doi.org/10.1242/jcs.61.1.31.
1120 Foe, V.E. 1989. "Mitotic Domains Reveal Early Commitment of Cells in Drosophila Embryos." *Trends in*
1121 *Genetics* 5 (C): 322. https://doi.org/10.1016/0168-9525(89)90120-0.
1122 Frydenberg, Jane, A. A. Hoffmann, and Volker Loeschcke. 2003. "DNA Sequence Variation and Latitudinal
1123 Associations in Hsp23, Hsp26 and Hsp27 from Natural Populations of Drosophila Melanogaster."
1124 *Molecular Ecology* 12 (8): 2025–32. https://doi.org/10.1046/j.1365-294X.2002.01882.x.
1125 Graham, John M. 2020. "Update on the Gestational Effects of Maternal Hyperthermia." *Birth Defects*
1126 *Research* 112 (12): 943–52. https://doi.org/10.1002/bdr2.1696.
1127 Graveley, Brenton R., Angela N. Brooks, Joseph W. Carlson, Michael O. Duff, Jane M. Landolin, Li Yang, Carlo
1128 G. Artieri, et al. 2011. "The Developmental Transcriptome of Drosophila Melanogaster." *Nature* 471
1129 (7339): 473–79. https://doi.org/10.1038/nature09715.
1130 Graziosi, G., F. Micali, R. Marzari, F. de Cristini, and A. Savoini. 1980. "Variability of Response of
1131 EarlyDrosophila Embryos to Heat Shock." *Journal of Experimental Zoology* 214 (2): 141–45.
1132 https://doi.org/10.1002/jez.1402140203.
1133 Harris, Tony J C, and Mark Peifer. 2004. "Adherens Junction-Dependent and -Independent Steps in the
1134 Establishment of Epithelial Cell Polarity in Drosophila." *The Journal of Cell Biology* 167 (1): 135–47.
1135 https://doi.org/10.1083/jcb.200406024.
1136 Herbert, Sébastien, Léo Valon, Laure Mancini, Nicolas Dray, Paolo Caldarelli, Jérôme Gros, Elric Esposito, et
1137 al. 2021. "LocalZProjector and DeProj: A Toolbox for Local 2D Projection and Accurate Morphometrics
1138 of Large 3D Microscopy Images." *BMC Biology* 19 (1): 136. https://doi.org/10.1186/s12915-021-
1139 01037-w.
1140 IPBES. 2019. *The Global Assessment Report of the Intergovernmental Science-Policy Platform on Biodiversity*
1141 *and Ecosystem Services*. https://doi.org/10.5281/zenodo.3831673.
1142 Kapun, Martin, Maite G Barrón, Fabian Staubach, Darren J. Obbard, R Axel W Wiberg, Jorge Vieira, Clément
1143 Goubert, et al. 2020. "Genomic Analysis of European Drosophila Melanogaster Populations Reveals
1144 Longitudinal Structure, Continent-Wide Selection, and Previously Unknown DNA Viruses." *Molecular*
1145 *Biology and Evolution* 37 (9): 2661–78. https://doi.org/10.1093/molbev/msaa120.
1146 Khoury, Mark J., and David Bilder. 2020. "Distinct Activities of Scrib Module Proteins Organize Epithelial
1147 Polarity." *Proceedings of the National Academy of Sciences of the United States of America* 117 (21):
1148 11531–40. https://doi.org/10.1073/pnas.1918462117.
1149 ———. 2022. "Minimal Functional Domains of the Core Polarity Regulator Dlg." *Biology Open* 11 (7).
1150 https://doi.org/10.1242/bio.059408.
1151 Kolaczkowski, Bryan, Andrew D. Kern, Alisha K. Holloway, and David J. Begun. 2011. "Genomic
1152 Differentiation between Temperate and Tropical Australian Populations of Drosophila Melanogaster."
1153 *Genetics* 187 (1): 245–60. https://doi.org/10.1534/genetics.110.123059.
1154 Kuntz, Steven G., and Michael B. Eisen. 2014. "Drosophila Embryogenesis Scales Uniformly across
1155 Temperature in Developmentally Diverse Species." *PLoS Genetics* 10 (4): e1004293.
1156 https://doi.org/10.1371/journal.pgen.1004293.
1157 ———. 2015. "Oxygen Changes Drive Non-Uniform Scaling in Drosophila Melanogaster Embryogenesis."

1158 *F1000Research* 4 (May): 1102. https://doi.org/10.12688/f1000research.7221.1.
1159 Lecuit, Thomas, and Alpha S. Yap. 2015. "E-Cadherin Junctions as Active Mechanical Integrators in Tissue
1160 Dynamics." *Nature Cell Biology* 17 (5): 533–39. https://doi.org/10.1038/ncb3136.
1161 Lemke, Steffen, Girish Kale, and Silvia Urbansky. 2020. "Comparing Gastrulation in Flies: Links between Cell
1162 Biology and the Evolution of Embryonic Morphogenesis." *Mechanisms of Development* 164 (October):
1163 103648. https://doi.org/10.1016/j.mod.2020.103648.
1164 Lockwood, Brent L., Cole R. Julick, and Kristi L. Montooth. 2017. "Maternal Loading of a Small Heat Shock
1165 Protein Increases Embryo Thermal Tolerance in Drosophila Melanogaster." *The Journal of*
1166 *Experimental Biology* 220 (Pt 23): 4492–4501. https://doi.org/10.1242/jeb.164848.
1167 Lu, Xuemin, Jennifer M. Li, Olivier Elemento, Saeed Tavazoie, and Eric F. Wieschaus. 2009. "Coupling of
1168 Zygotic Transcription to Mitotic Control at the Drosophila Mid-Blastula Transition." *Development*
1169 *(Cambridge, England)* 136 (12): 2101–10. https://doi.org/10.1242/dev.034421.
1170 Lynch, Jeremy A., Ezzat El-Sherif, and Susan J. Brown. 2012. "Comparisons of the Embryonic Development
1171 of Drosophila , Nasonia , and Tribolium." *Wiley Interdisciplinary Reviews: Developmental Biology* 1 (1):
1172 16–39. https://doi.org/10.1002/wdev.3.
1173 Machado, Heather E., Alan O. Bergland, Katherine R. O'Brien, Emily L. Behrman, Paul S. Schmidt, and Dmitri
1174 A. Petrov. 2016. "Comparative Population Genomics of Latitudinal Variation in Drosophila Simulans
1175 and Drosophila Melanogaster." *Molecular Ecology* 25 (3): 723–40.
1176 https://doi.org/10.1111/mec.13446.
1177 Mapelli, Marina, and Cayetano Gonzalez. 2012. "On the Inscrutable Role of Inscuteable: Structural Basis
1178 and Functional Implications for the Competitive Binding of NuMA and Inscuteable to LGN." *Open*
1179 *Biology* 2 (8): 120102. https://doi.org/10.1098/rsob.120102.
1180 Martin, Adam C. 2020. "The Physical Mechanisms of Drosophila Gastrulation: Mesoderm and Endoderm
1181 Invagination." *Genetics* 214 (3): 543–60. https://doi.org/10.1534/genetics.119.301292.
1182 Mazumdar, Aveek, and Manjari Mazumdar. 2002. "How One Becomes Many: Blastoderm Cellularization in
1183 Drosophila Melanogaster." *BioEssays : News and Reviews in Molecular, Cellular and Developmental*
1184 *Biology* 24 (11): 1012–22. https://doi.org/10.1002/bies.10184.
1185 McCartney, Brooke M., Donald G. McEwen, Elizabeth Grevengoed, Paul Maddox, Amy Bejsovec, and Mark
1186 Peifer. 2001. "Drosophila APC2 and Armadillo Participate in Tethering Mitotic Spindles to Cortical
1187 Actin." *Nature Cell Biology* 3 (10): 933–38. https://doi.org/10.1038/ncb1001-933.
1188 McColl, Gawain, and Stephen W. McKechnie. 1999. "The Drosophila Heat Shock Hsr-Omega Gene: An Allele
1189 Frequency Cline Detected by Quantitative PCR." *Molecular Biology and Evolution* 16 (11): 1568–74.
1190 https://doi.org/10.1093/oxfordjournals.molbev.a026069.
1191 Miller, Morton W., and Charles C. Church. 2013. "Arrhenius Thermodynamics and Birth Defects: Chemical
1192 Teratogen Synergy. Untested, Testable, and Projected Relevance." *Birth Defects Research. Part C,*
1193 *Embryo Today : Reviews* 99 (1): 50–60. https://doi.org/10.1002/bdrc.21025.
1194 Oakeshott, J. G., S. W. McKechnie, and G. K. Chambers. 1984. "Population Genetics of the Metabolically
1195 Related Adh, Gpdh and Tpi Polymorphisms in Drosophila Melanogaster I. Geographic Variation in
1196 Gpdh and Tpi Allele Frequencies in Different Continents." *Genetica* 63 (1): 21–29.
1197 https://doi.org/10.1007/BF00137461.
1198 Paaby, Annalise B., Alan O. Bergland, Emily L. Behrman, and Paul S. Schmidt. 2014. "A Highly Pleiotropic
1199 Amino Acid Polymorphism in the Drosophila Insulin Receptor Contributes to Life-History Adaptation."
1200 *Evolution; International Journal of Organic Evolution* 68 (12): 3395–3409.
1201 https://doi.org/10.1111/evo.12546.
1202 Pietzsch, Tobias, Stephan Saalfeld, Stephan Preibisch, and Pavel Tomancak. 2015. "BigDataViewer:
1203 Visualization and Processing for Large Image Data Sets." *Nature Methods* 12 (6): 481–83.
1204 https://doi.org/10.1038/nmeth.3392.
1205 Preibisch, Stephan, Stephan Saalfeld, and Pavel Tomancak. 2009. "Globally Optimal Stitching of Tiled 3D
1206 Microscopic Image Acquisitions." *Bioinformatics (Oxford, England)* 25 (11): 1463–65.
1207 https://doi.org/10.1093/bioinformatics/btp184.
1208 Pritchard, David K., and Gerold Schubiger. 1996. "Activation of Transcription in Drosophila Embryos Is a
1209 Gradual Process Mediated by the Nucleocytoplasmic Ratio." *Genes & Development* 10 (9): 1131–42.
1210 https://doi.org/10.1101/gad.10.9.1131.

1211 Raguso, Robert A. 2020. “Don’t Forget the Flies: Dipteran Diversity and Its Consequences for Floral Ecology
1212 and Evolution.” *Applied Entomology and Zoology* 55 (1): 1–7. https://doi.org/10.1007/s13355-020-
1213 00668-9.
1214 Rand, David M., Daniel M. Weinreich, Daniel Lerman, Donna Folk, and George W. Gilchrist. 2010. “Three
1215 Selections Are Better than One: Clinal Variation of Thermal QTL from Independent Selection
1216 Experiments in Drosophila.” *Evolution* 64 (10): 2921–34. https://doi.org/10.1111/j.1558-
1217 5646.2010.01039.x.
1218 Rim, Ellen Youngsoo, Hans Clevers, and Roel Nusse. 2022. “The Wnt Pathway: From Signaling Mechanisms
1219 to Synthetic Modulators.” *Annual Review of Biochemistry* 91 (June): 571–98.
1220 https://doi.org/10.1146/annurev-biochem-040320-103615.
1221 Rizzelli, Francesca, Maria Grazia Malabarba, Sara Sigismund, and Marina Mapelli. 2020. “The Crosstalk
1222 between Microtubules, Actin and Membranes Shapes Cell Division.” *Open Biology* 10 (3): 190314.
1223 https://doi.org/10.1098/rsob.190314.
1224 Rudman, Seth M., Sharon I. Greenblum, Subhash Rajpurohit, Nicolas J. Betancourt, Jinjoo Hanna, Susanne
1225 Tilk, Tuya Yokoyama, Dmitri A. Petrov, and Paul S. Schmidt. 2022. “Direct Observation of Adaptive
1226 Tracking on Ecological Time Scales in Drosophila.” *Science (New York, N.Y.)* 375 (6586): eabj7484.
1227 https://doi.org/10.1126/science.abj7484.
1228 Rutherford, Suzanne L., and Susan Lindquist. 1998. “Hsp90 as a Capacitor for Morphological Evolution.”
1229 *Nature* 396 (6709): 336–42. https://doi.org/10.1038/24550.
1230 Sangster, Todd A., Susan Lindquist, and Christine Queitsch. 2004. “Under Cover: Causes, Effects and
1231 Implications of Hsp90-Mediated Genetic Capacitance.” *BioEssays : News and Reviews in Molecular,*
1232 *Cellular and Developmental Biology* 26 (4): 348–62. https://doi.org/10.1002/bies.20020.
1233 Sawyer, Lesley A., Federica Sandrelli, Carlo Pasetto, Alexandre A. Peixoto, Ezio Rosato, Rodolfo Costa, and
1234 Charalambos P. Kyriacou. 2006. “The Period Gene Thr-Gly Polymorphism in Australian and African
1235 Drosophila Melanogaster Populations: Implications for Selection.” *Genetics* 174 (1): 465–80.
1236 https://doi.org/10.1534/genetics.106.058792.
1237 Schmidt, Anja, and Jörg Grosshans. 2018. “Dynamics of Cortical Domains in Early Drosophila Development.”
1238 *Journal of Cell Science* 131 (7). https://doi.org/10.1242/jcs.212795.
1239 Schmidt, Paul S., David D. Duvernell, and Walter F. Eanes. 2000. “Adaptive Evolution of a Candidate Gene
1240 for Aging in Drosophila.” *Proceedings of the National Academy of Sciences of the United States of*
1241 *America* 97 (20): 10861–65. https://doi.org/10.1073/pnas.190338897.
1242 Schmidt, Paul S., and Annalise B. Paaby. 2008. “Reproductive Diapause and Life-History Clines in North
1243 American Populations of Drosophila Melanogaster.” *Evolution* 62 (5): 1204–15.
1244 https://doi.org/10.1111/j.1558-5646.2008.00351.x.
1245 Sezgin, Efe, David D. Duvernell, Luciano M. Matzkin, Yihao Duan, Chen Tseh Zhu, Brian C. Verrelli, and
1246 Walter F. Eanes. 2004. “Single-Locus Latitudinal Clines and Their Relationship to Temperate
1247 Adaptation in Metabolic Genes and Derived Alleles in Drosophila Melanogaster.” *Genetics* 168 (2):
1248 923–31. https://doi.org/10.1534/genetics.104.027649.
1249 Telley, Ivo A., Imre Gáspár, Anne Ephrussi, and Thomas Surrey. 2012. “Aster Migration Determines the
1250 Length Scale of Nuclear Separation in the Drosophila Syncytial Embryo.” *The Journal of Cell Biology*
1251 197 (7): 887–95. https://doi.org/10.1083/jcb.201204019.
1252 Umina, P. A., A. R. Weeks, M. R. Kearney, S. W. McKechnie, and A. A. Hoffmann. 2005. “Evolution: A Rapid
1253 Shift in a Classic Clinal Pattern in Drosophila Reflecting Climate Change.” *Science* 308 (5722): 691–93.
1254 https://doi.org/10.1126/science.1109523.
1255 Vazquez, Julio, Daniel Pauli, and Alfred Tissières. 1993. “Transcriptional Regulation in Drosophila during
1256 Heat Shock: A Nuclear Run-on Analysis.” *Chromosoma* 102 (4): 233–48.
1257 https://doi.org/10.1007/BF00352397.
1258 Verrelli, B. C., and W. F. Eanes. 2001. “Clinal Variation for Amino Acid Polymorphisms at the Pgm Locus in
1259 Drosophila Melanogaster.” *Genetics* 157 (4): 1649–63. https://doi.org/10.1093/genetics/157.4.1649.
1260 Vigue, C. L., and F. M. Johnson. 1973. “Isozyme Variability in Species of the Genus Drosophila. VI.
1261 Frequency-Property-Environment Relationships of Allelic Alcohol Dehydrogenases in D.
1262 Melanogaster.” *Biochemical Genetics* 9 (3): 213–27.
1263 Walter, Marika F., Nancy S. Petersen, and Harald Biessmann. 1990. “Heat Shock Causes the Collapse of the

1264 Intermediate Filament Cytoskeleton in Drosophila Embryos." *Developmental Genetics* 11 (4): 270–79.
1265 https://doi.org/10.1002/dvg.1020110405.
1266 Weeks, A. R., S. W. Mckechnie, and A. A. Hoffmann. 2006. "In Search of Clinal Variation in the Period and
1267 Clock Timing Genes in Australian Drosophila Melanogaster Populations." *Journal of Evolutionary*
1268 *Biology* 19 (2): 551–57. https://doi.org/10.1111/j.1420-9101.2005.01013.x.
1269 Welte, Michael A., Joan M. Tetrault, Robert P. Dellavalle, and Susan L. Lindquist. 1993. "A New Method for
1270 Manipulating Transgenes: Engineering Heat Tolerance in a Complex, Multicellular Organism." *Current*
1271 *Biology* 3 (12): 842–53. https://doi.org/10.1016/0960-9822(93)90218-D.
1272 Xie, Yi, and J. Todd Blankenship. 2018. "Differentially-Dimensioned Furrow Formation by Zygotic Gene
1273 Expression and the MBT." *PLoS Genetics* 14 (1): e1007174.
1274 https://doi.org/10.1371/journal.pgen.1007174.
1275 Zheng, Liuliu, Leonardo A. Sepúlveda, Rhonald C. Lua, Olivier Lichtarge, Ido Golding, and Anna Marie Sokac.
1276 2013. "The Maternal-to-Zygotic Transition Targets Actin to Promote Robustness during
1277 Morphogenesis." *PLoS Genetics* 9 (11): e1003901. https://doi.org/10.1371/journal.pgen.1003901.
1278

1279 **Figure 1**

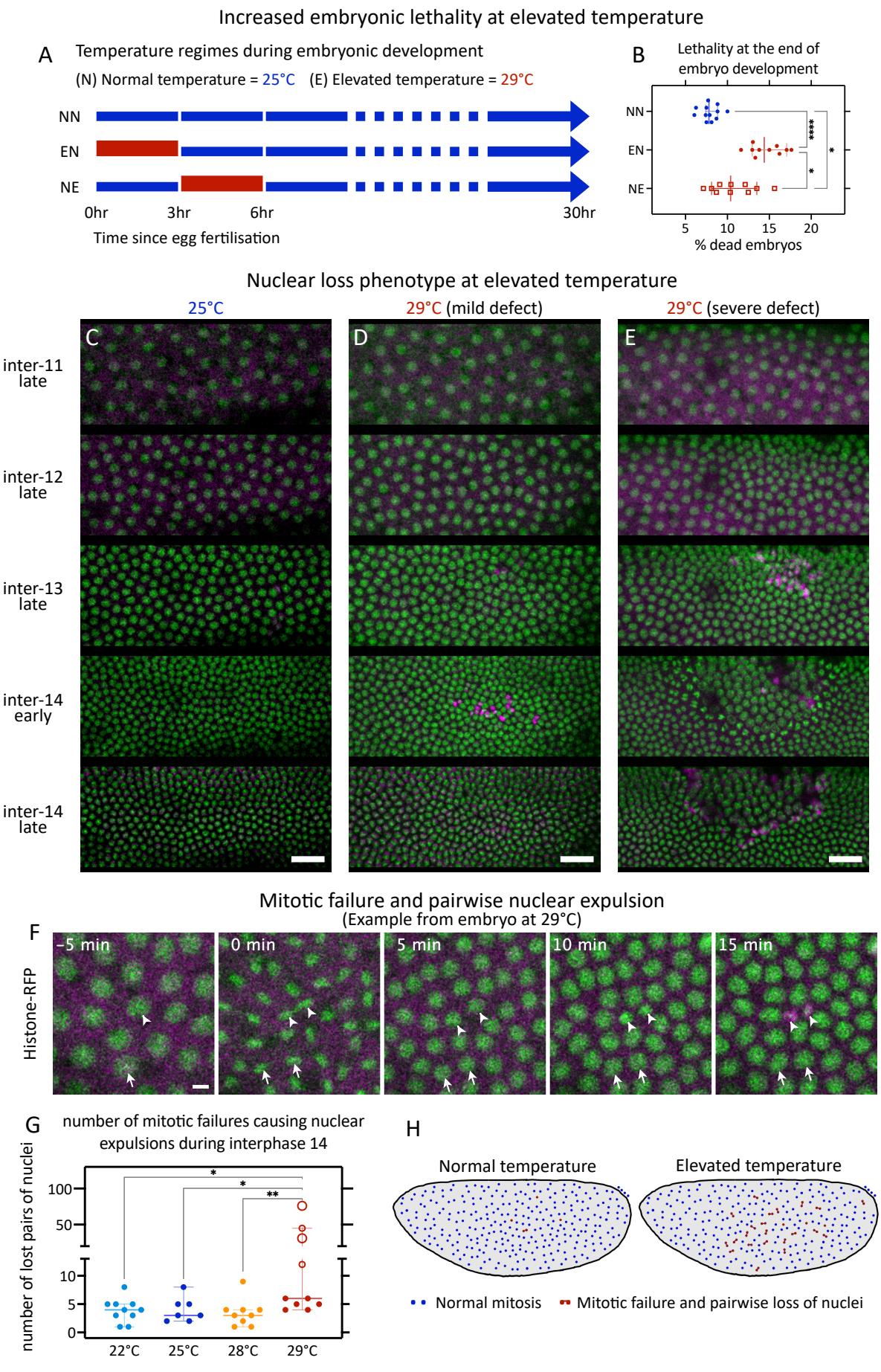

1280

1281 **Figure 2**

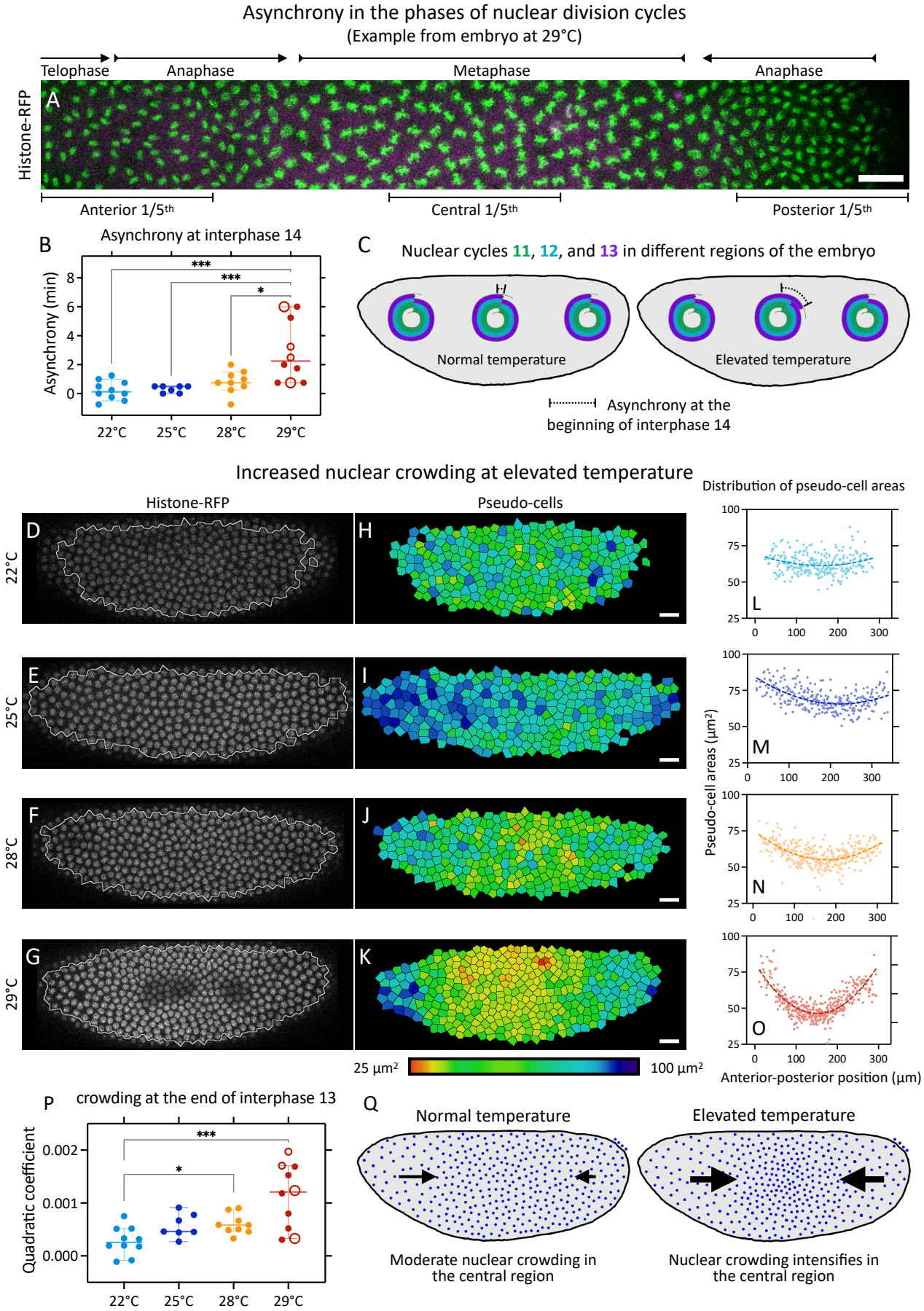

1282

1283 **Figure 3**

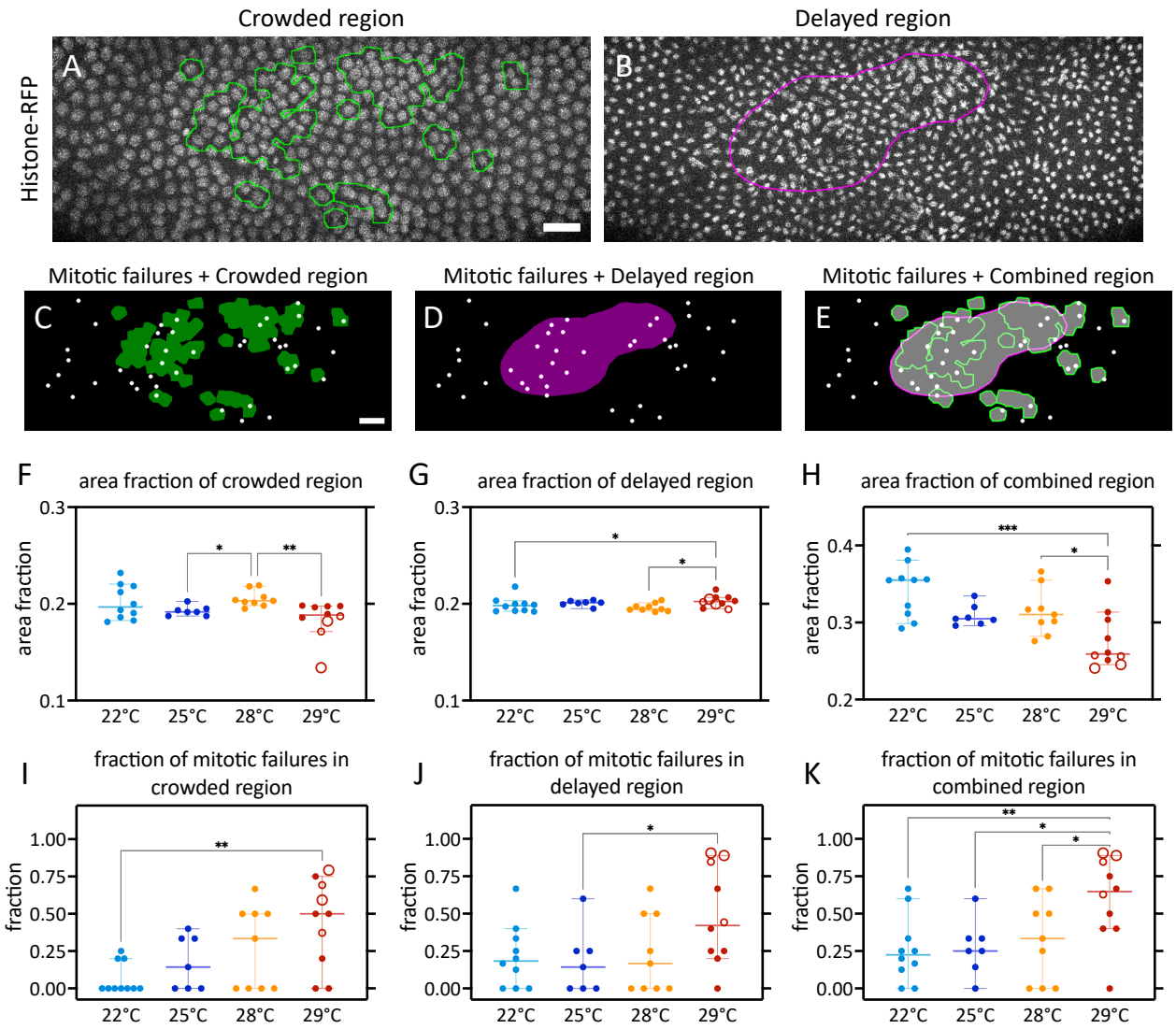

1284

1285 **Figure 4**

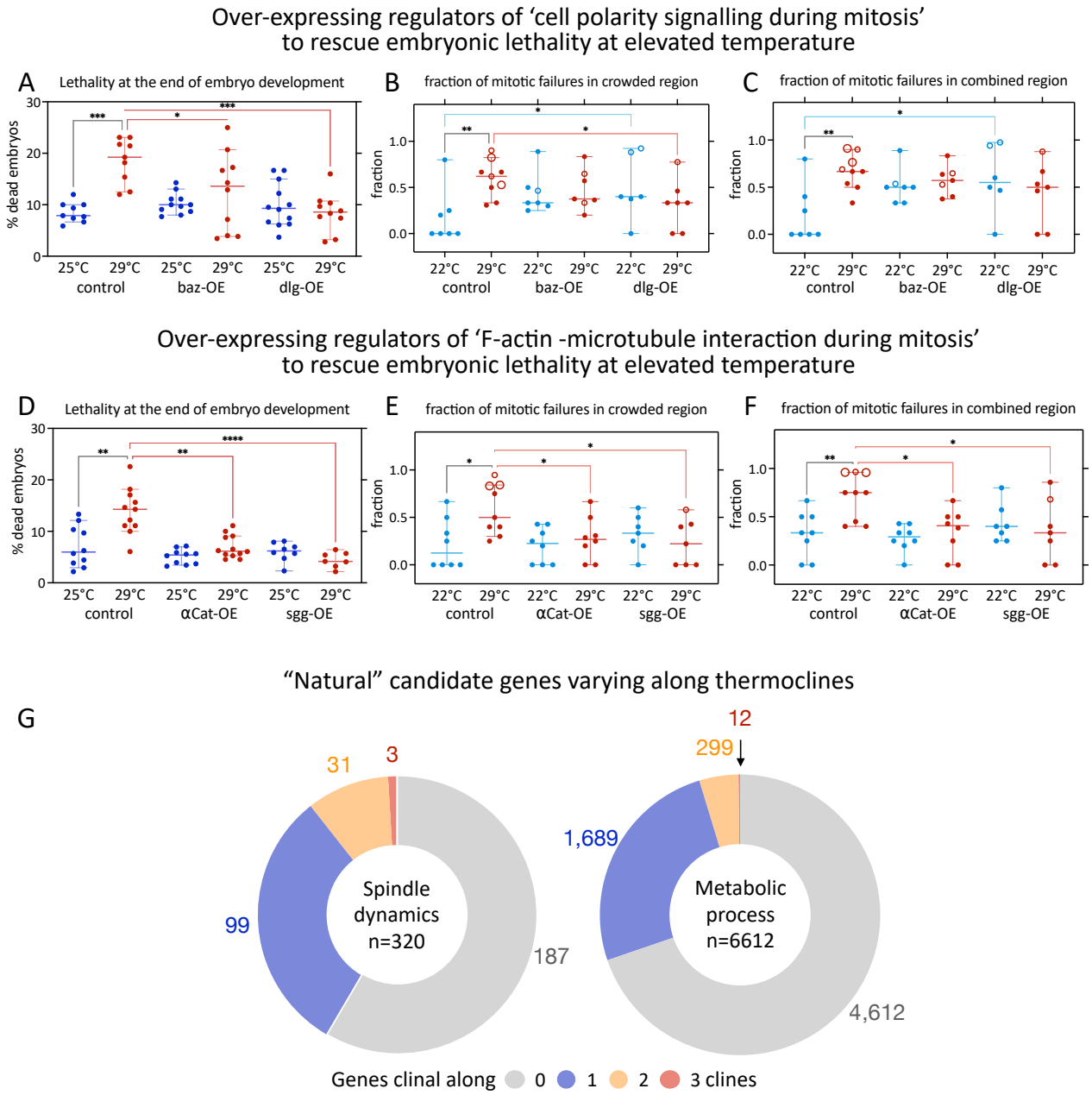

1286

1287 **Figure S1**

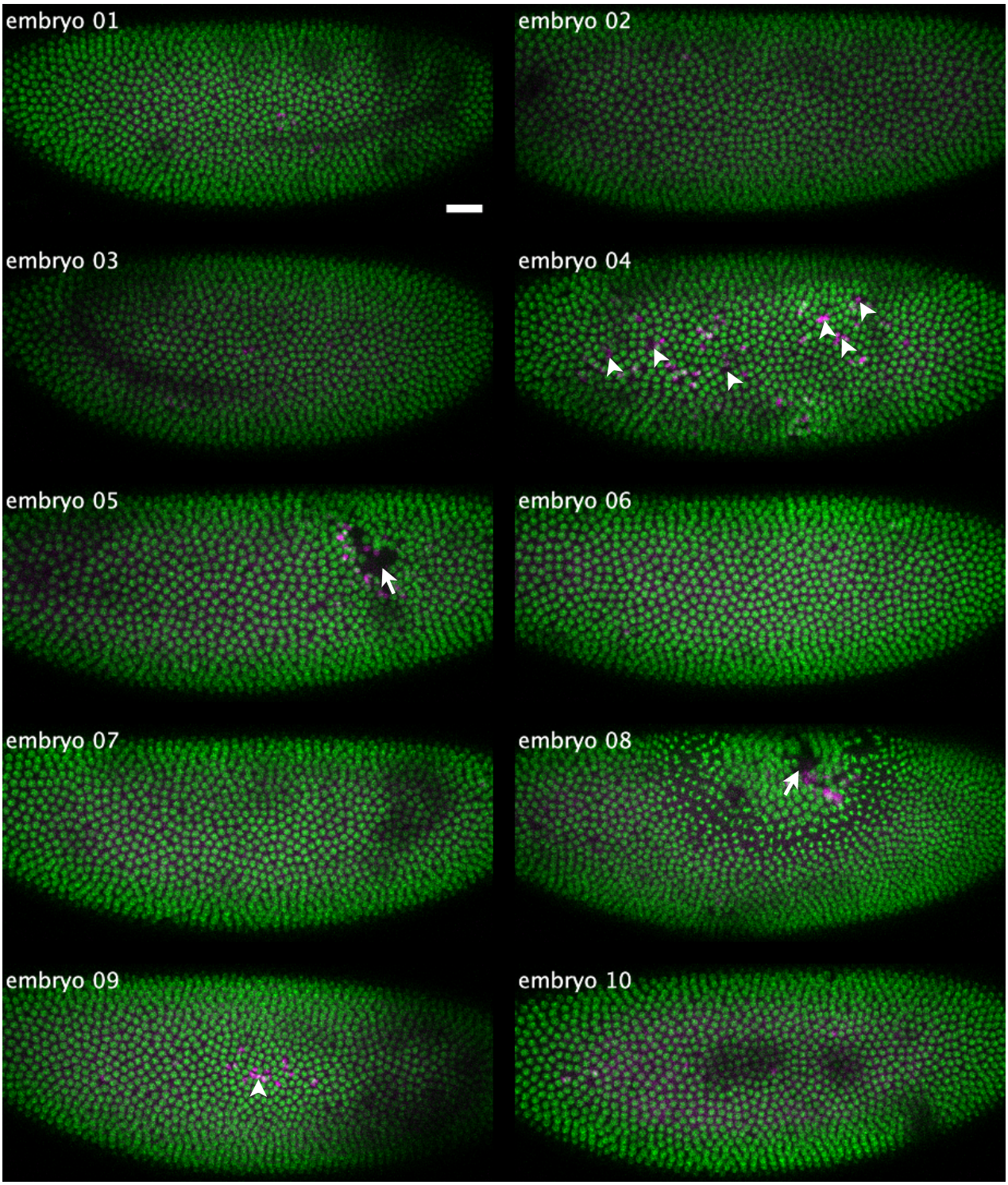

1288

1289 **Figure S2**

Nuclear loss phenotype due to elevated temperature

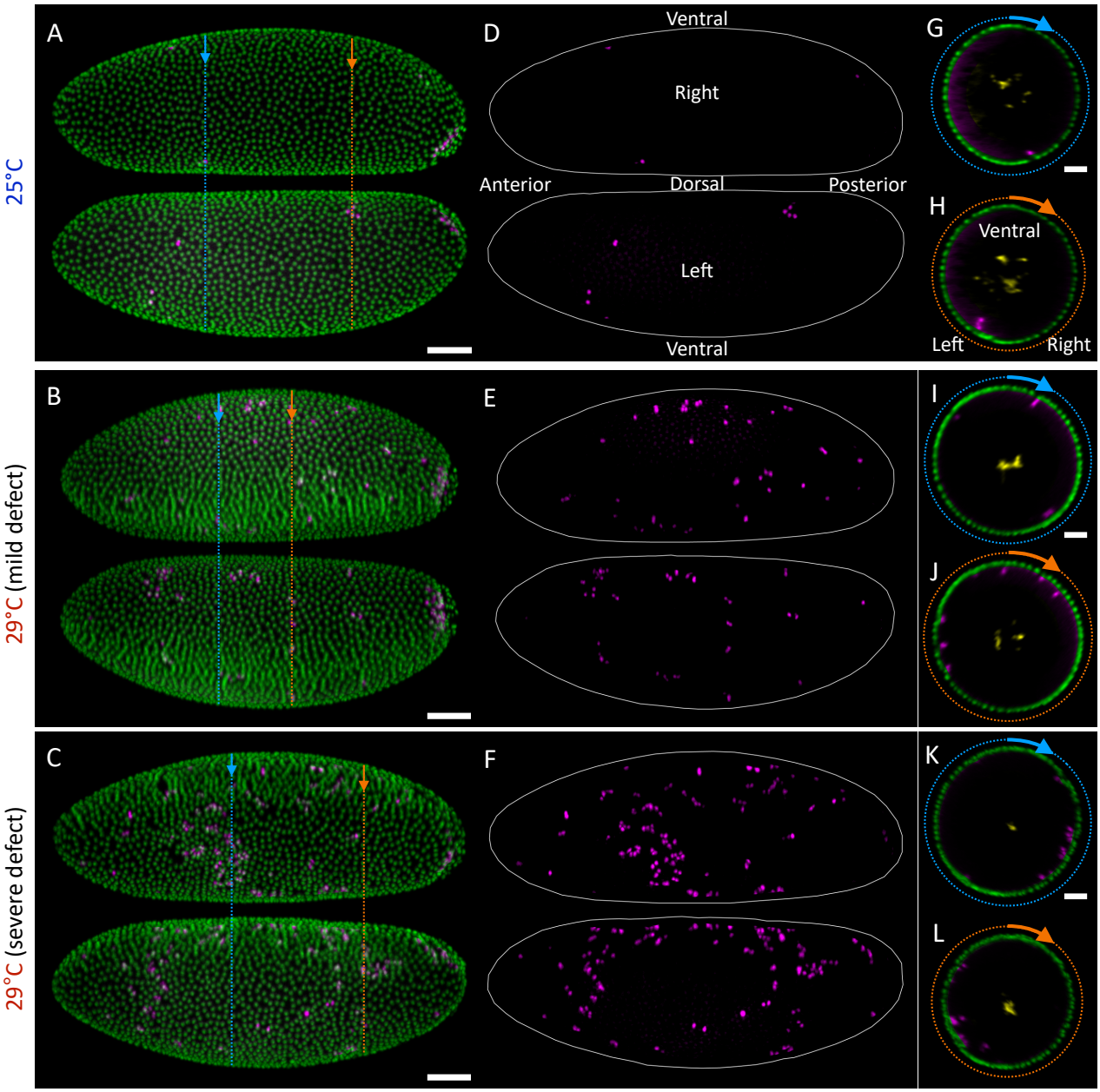

1290

1291 **Figure S3**

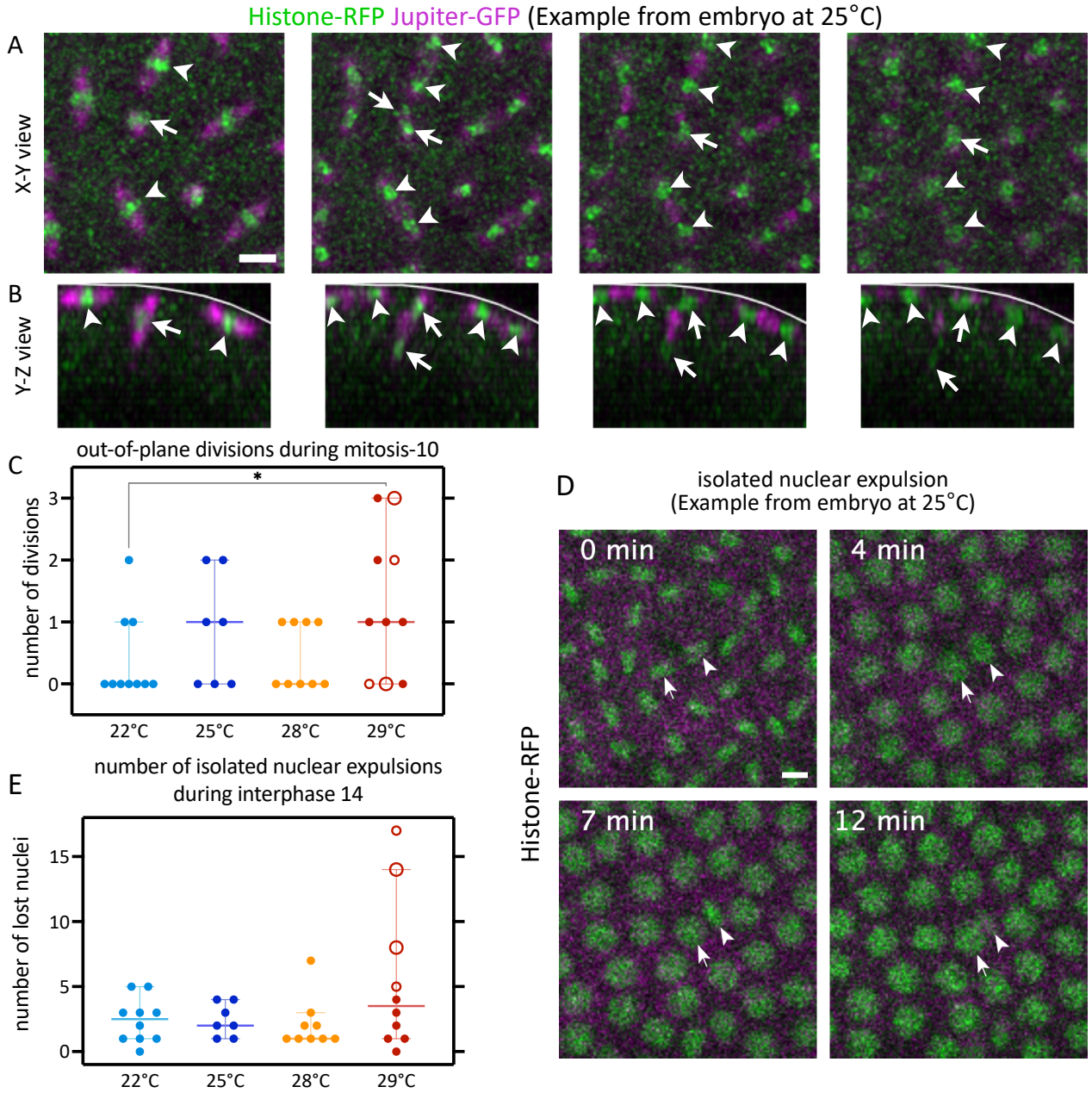

1292

1293 **Figure S4**

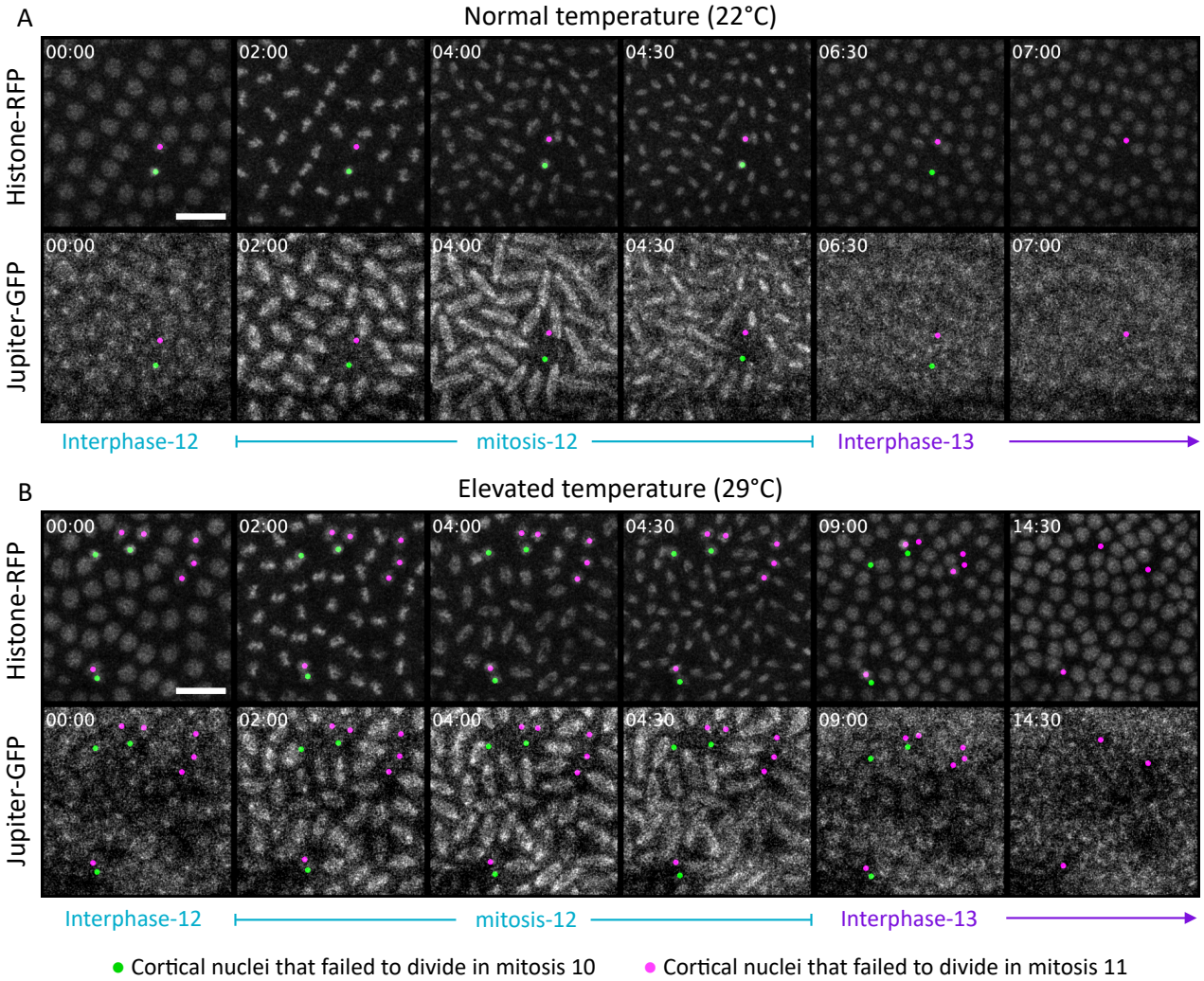

1294

Figure S5

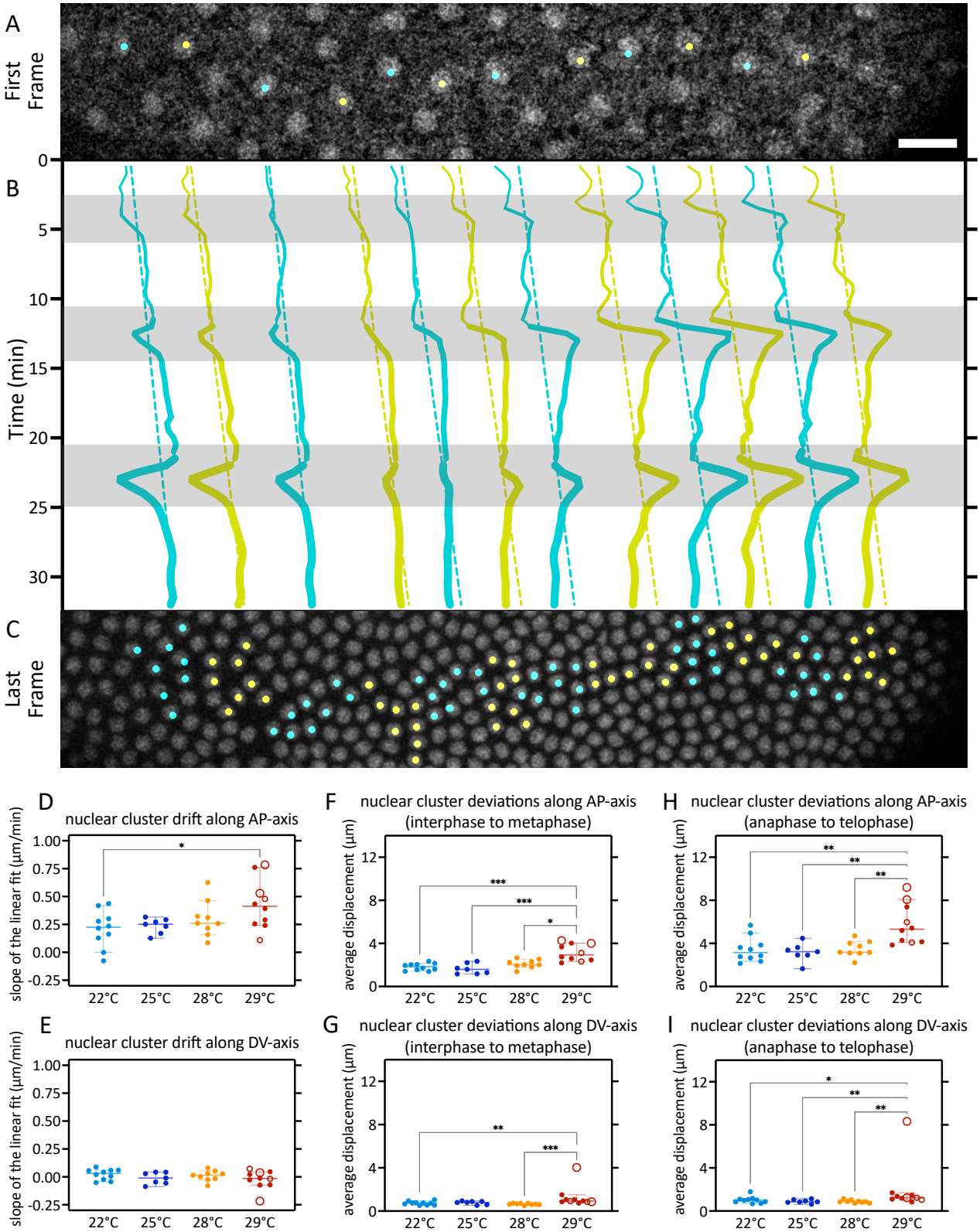
A
First Frame
B
Time (min)
0
5
10
15
20
25
30
C
Last Frame
D
nuclear cluster drift along AP-axis
slope of the linear fit (µm/min)
1.00
0.75
0.50
0.25
0.00
-0.25
22°C
25°C
28°C
29°C
E
nuclear cluster drift along DV-axis
F
nuclear cluster deviations along AP-axis (interphase to metaphase)
average displacement (µm)
G
nuclear cluster deviations along DV-axis (interphase to metaphase)
H
nuclear cluster deviations along AP-axis (anaphase to telophase)
I
nuclear cluster deviations along DV-axis (anaphase to telophase)

Figure S6

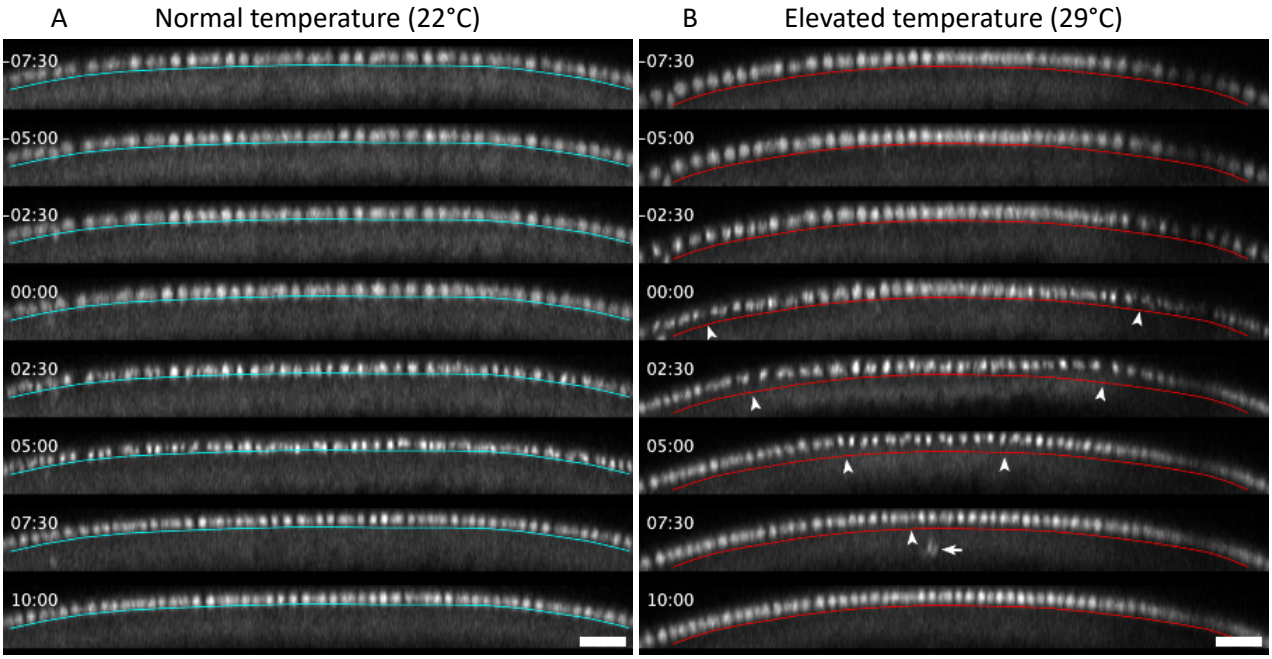
A
Normal temperature (22°C)
B
Elevated temperature (29°C)
-07:30
-05:00
-02:30
00:00
02:30
05:00
07:30
10:00
-07:30
-05:00
-02:30
00:00
02:30
05:00
07:30
10:00

1299 **Figure S7**

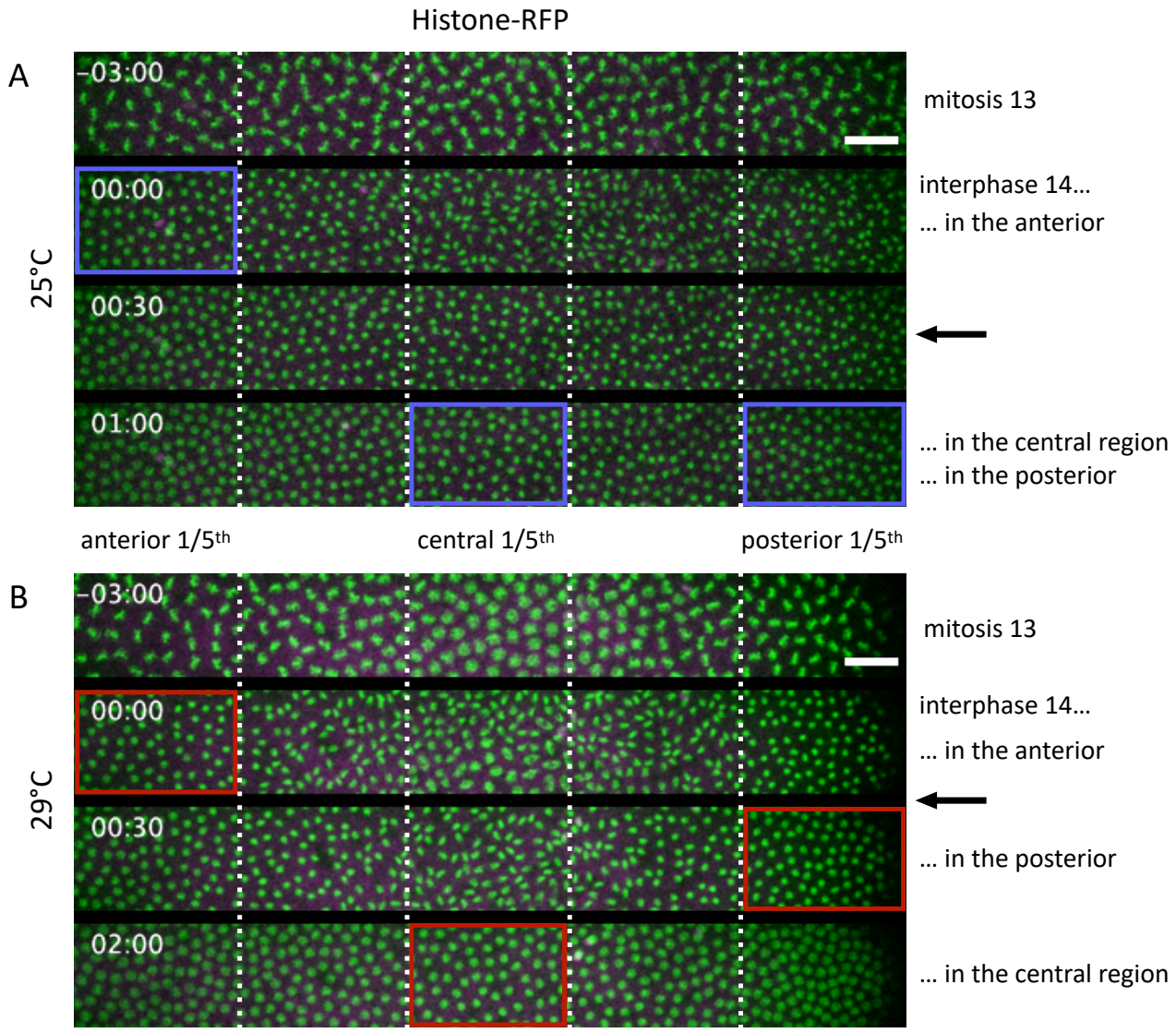

1300

Figure S8

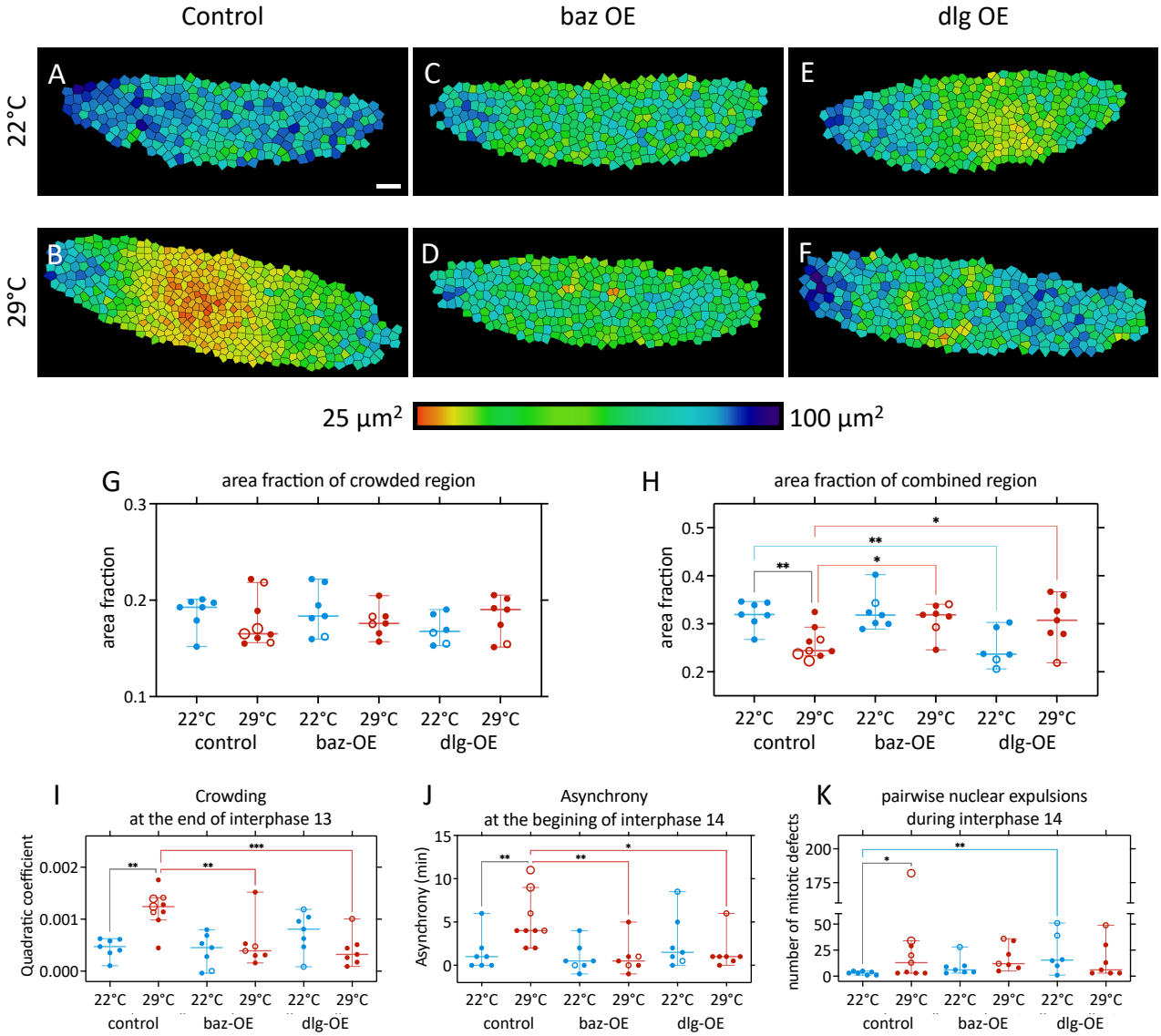
Control
baz OE
dlg OE
22°C
29°C
A
B
C
D
E
F
25 µm²
100 µm²
G
area fraction of crowded region
area fraction
H
area fraction of combined region
I
Crowding
at the end of interphase 13
Quadratic coefficient
J
Asynchrony
at the begining of interphase 14
Asynchrony (min)
K
pairwise nuclear expulsions
during interphase 14
number of mitotic defects
control
baz-OE
dlg-OE

1303 **Figure S9**

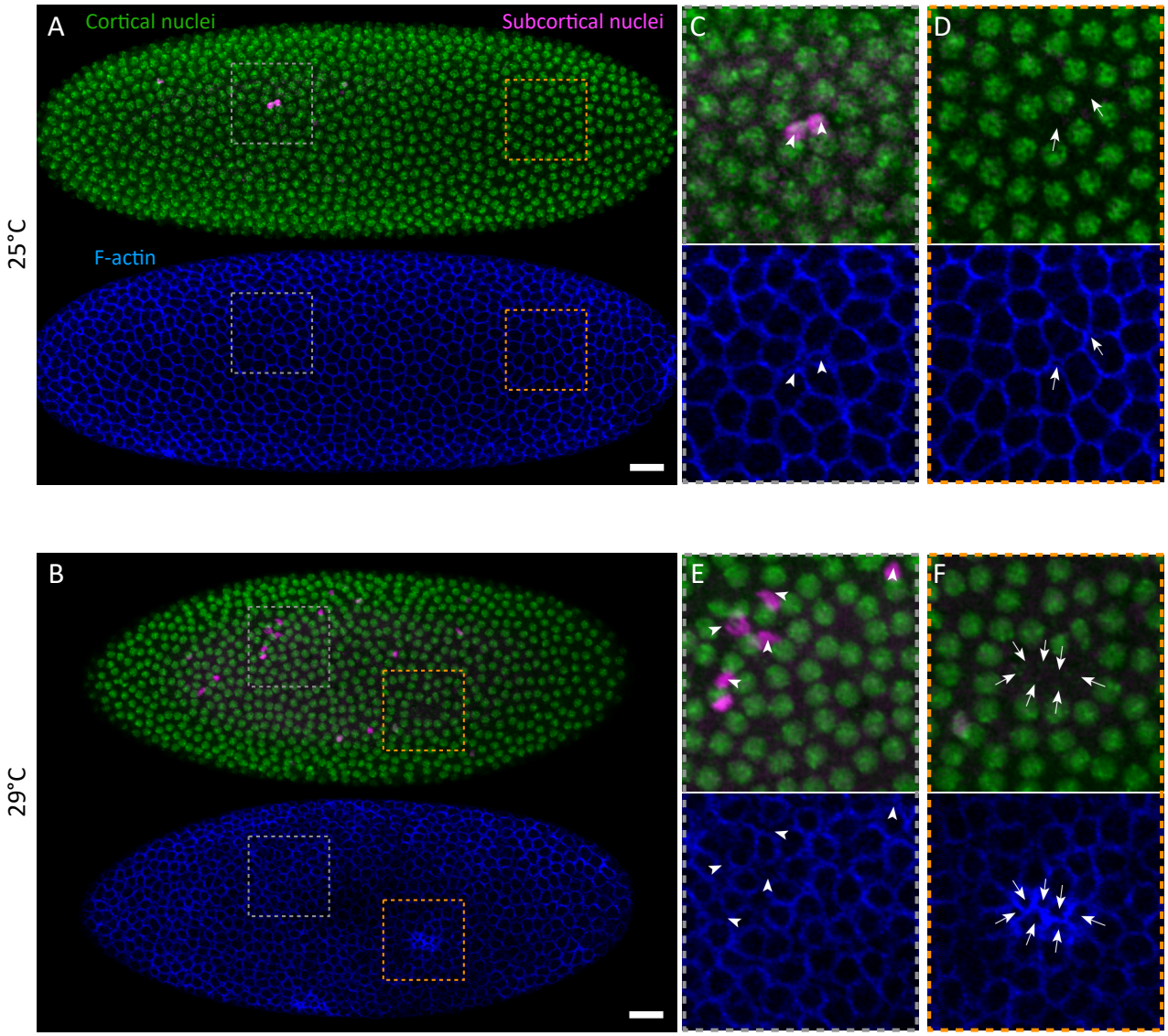

1304

1305 **Figure S10**

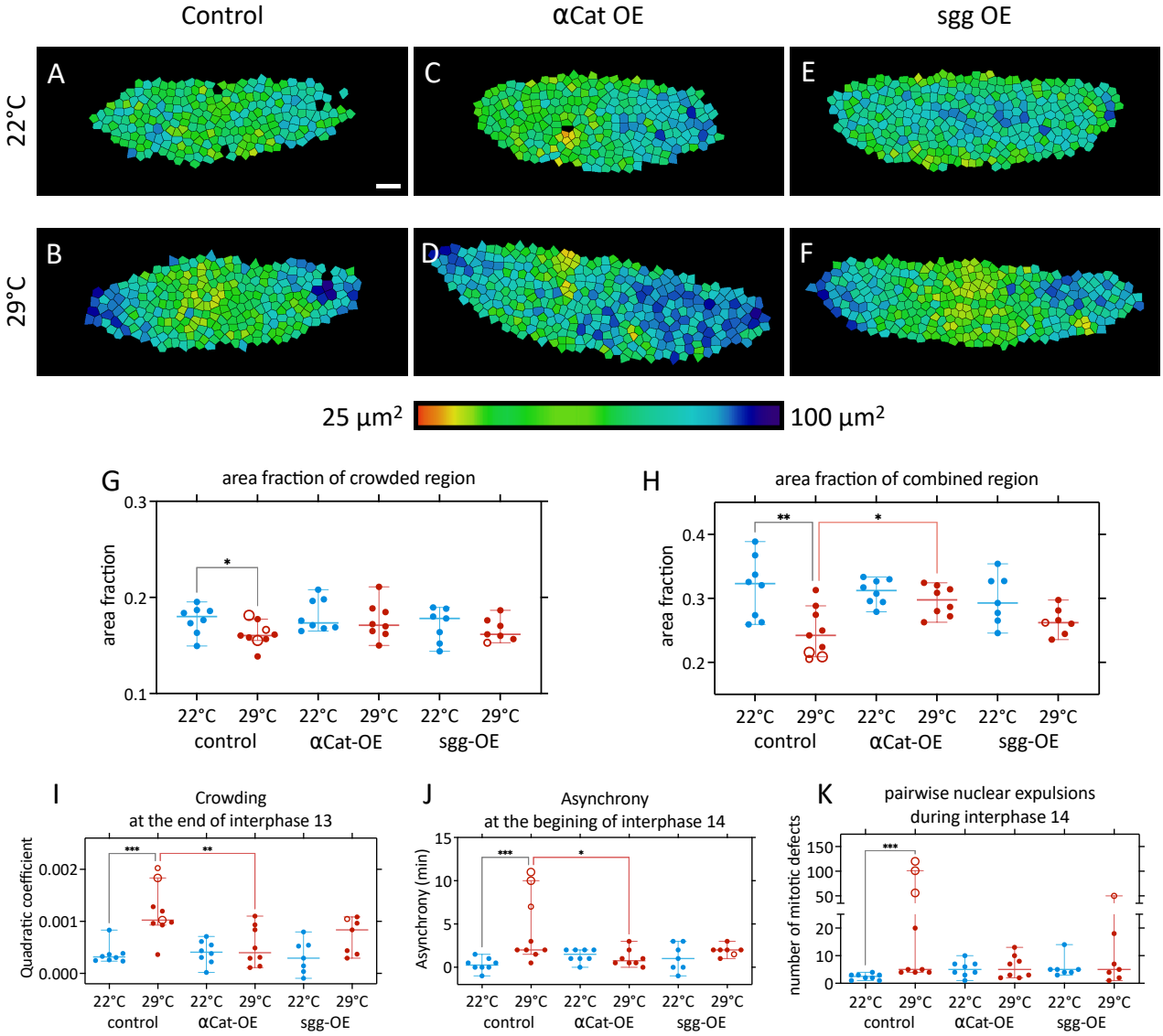

1306

1307 **Figure S11**

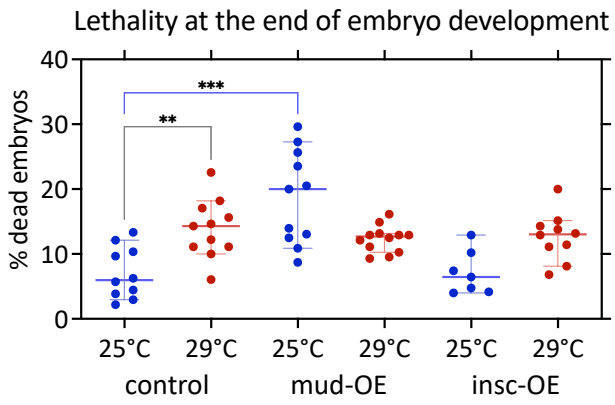

1308